Available online at www.sciencedirect.com

ScienceDirect

MATTER AND RADIATION AT EXTREMES

Matter and Radiation at Extremes 1 (2016) 59–75

www.journals.elsevier.com/matter-and-radiation-at-extremes

Recent advances in high-pressure science and technology

Ho-Kwang Mao*, Bin Chen, Jiuhua Chen, Kuo Li, Jung-Fu Lin, Wenge Yang, Haiyan Zheng

Center for High Pressure Science and Technology Advanced Research, Shanghai, 201203, PR China

Received 17 November 2015; revised 2 December 2015; accepted 2 December 2015
Available online 4 February 2016

Abstract

Recently we are witnessing the boom of high-pressure science and technology from a small niche field to becoming a major dimension in physical sciences. One of the most important technological advances is the integration of synchrotron nanotechnology with the minute samples at ultrahigh pressures. Applications of high pressure have greatly enhanced our understanding of the electronic, phonon, and doping effects on the newly emerged graphene and related 2D layered materials. High pressure has created exotic stoichiometry even in common Group 17, 15, and 14 compounds and drastically altered the basic σ and π bonding of organic compounds. Differential pressure measurements enable us to study the rheology and flow of mantle minerals in solid state, thus quantitatively constraining the geodynamics. They also introduce a new approach to understand defect and plastic deformations of nano particles. These examples open new frontiers of high-pressure research.

PACS: 74.62.Fj; 07.85.Qe; 31.15.ae; 83.50.-v

Keywords: High pressure science and technology; Static high pressure; Synchrotron X-ray probe; Equation of state

1. Introduction

High-pressure research has been advancing rapidly during the last decades, thanks to the concerted development of various pressure devices and probing technology. The migration of numerous dedicated synchrotron techniques to high-pressure research has greatly impacted fundamental physics, chemistry, Earth, and materials sciences.

Recent discoveries in high-pressure condensed matter physics include the metallization of hydrogen, quantum criticality, high T_c superconductors, polyamorphism, and exotic metals. High pressure can dramatically decrease the atomic volume and increase the electronic density of the reactants, which will result in novel and special chemical reactivity, kinetics and the reaction mechanisms. Particularly noticeable are the pressure induced transitions in elements, molecular compounds, ionic compounds, and high pressure chemistry reaction assisted by photochemistry and electrochemistry. The rheological properties of Earth and planetary materials can now be well characterized with controlled strain rate at high pressures using synchrotron X-ray diffraction and imaging. The dislocation and grain rotation of nanomaterials can be quantitatively studied with pressure tuning.

The impact of the pressure dimension has expanded rapidly to cover a wide domain of physical sciences. It will not be possible to have a comprehensive coverage of the entire frontiers in this article. Instead, we will focus on the advances of several selected areas of great potentials, and present short summaries, highlights, and recent developments. Moreover, the subjects will be limited mostly to static compressions.

2. High-pressure synchrotron X-ray probes

High pressure is a technology dictated science. Over the century-long development of high-pressure technology, record

* Corresponding author.
E-mail address: maohk@hpstar.ac.cn (H.-K. Mao).
Peer review under responsibility of Science and Technology Information Center, China Academy of Engineering Physics.

http://dx.doi.org/10.1016/j.mre.2016.01.005

pressures doubling that at the center of the Earth [1] can be reached with a minute amount of sample. Synchrotron developments have been one of the major driving forces for the recent breakout of high pressure activities [2]. By taking advantage of the third generation synchrotron sources and fast advanced X-ray optics development, high pressure community has benefited from various techniques to a new level of high pressure studies: like the high brilliance for ultra small focused beam [3], tunability for spectroscopy and resonant scattering [4], circular and linear polarization for magnetic study [5], high energy resolution inelastic scattering for dynamical properties [6], coherence imaging for ultra-sensitive phase contrast for even very light materials at tens of nanometer scale [7], high energy scattering for disordered system, amorphous and liquid phases [8], etc. Traditional high-pressure study mainly focused on the static study, the time-resolved techniques will allow us to study material behavior far from equilibrium and have snap shot during the dynamic process. It is the golden time for integrating these advanced techniques coherently to solve the real world complicated system and understand the materials behavior under extreme environment from all aspects to achieve ground-breaking results. Here we focus on a few highlight works with these advanced probes.

2.1. Local ordering from sub-nanometer resolution with high-energy X-ray diffraction

Under high pressure, material usually consists of highly deformed pieces and turns to very fine crystallites, which causes the severe broadening of X-ray powder diffraction peaks. Although Scherrer equation can be used to de-convolute the strain and particle size effect from the diffraction peak width vs. diffraction angle, it is often hard to distinguish the heavy deformation of nanoparticle from the amorphous states. Atomic resolution transmission electron microscopy has been used as the major tool to probe the microstructure with resolution at sub-nanometer and even sub-angstrom scale from direct high resolution imaging technique. High-energy X-ray diffraction from the other end provides wider Q-coverage (reciprocal space) diffraction information, and upon the Fourier transformation, one can obtain the real space pair distribution function (PDF) distribution at atomic bonding distances. For nano- and amorphous-materials research under high pressure, the high energy PDF study would provide a unique characteristic tool to understand the deformation mechanism and structure stability at atomic scale. For the case of nano-sized Y_2O_3 particles, there is a critical size effect discovered with the PDF tools [9], where 16 nm Y_2O_3 shows totally different structure stability and phase transition route comparing to 21 nm Y_2O_3 particle, while the latter one behaves in the same way as bulk materials. Ta_2O_5 has a unique crystal structure with a very long a lattice comparing to the other axes ($a = 43.997$ Å, $b = 3.894$ Å, $c = 6.209$ Å with a Pmm2 space group) [10]. Looking at the bonding structure along a, there are several weak bonded connections. High energy PDF was applied to the in-situ high pressure structure study, and clear local bonding breakage can be seen at different pressure stage (Fig. 1). For comparing with the traditional atomic resolution TEM characterization, samples recovered from different pressure stages were checked with TEM, and the clear local order/disorder atomic re-arrangement can be seen which matches the PDF study very well [10], in which combining the traditional TEM probe, high energy PDF demonstrates the super powerful capability for the in-situ local bonding (sub nanometer) order/disorder characterization.

2.2. Nanoscale deformation imaging with the coherent scattering probe

The evolution of morphology and internal strain under high pressure fundamentally alters the physical property, structural stability, phase transition and deformation mechanism of materials. Until now, only averaged strain distributions have been studied. To improve our fundamental understanding of the deformation mechanism, we need to probe individual nano grains under extreme conditions. For doing so, a much higher spatial resolution probe is required. The Bragg coherent X-ray diffraction imaging (CXDI) technique is a promising tool to probe the internal strain distribution and grain shape during the plastic/elastic deformation of individual nanometer-sized single crystals. Coherence diffraction can be realized by setting an entrance slit smaller than the transverse coherence length and an X-ray sensitive area detector at far field to catch the Fourier scattering with high resolution. The third-generation sources of synchrotron radiation using undulators and the upcoming multi-bend Achromat lattice upgrade for major large synchrotron sources have provided a great source to ensure coherence with a practical flux level to conduct experiment. As the coherent X-rays pass through a distorted crystal, both the scattering intensity and phase will be affected. Bragg CXDI operates by inverting three-dimensional (3D) diffraction patterns in the vicinity of Bragg peaks to real-space images using phase retrieval algorithms [11]. In the resulting images, the reconstructed magnitude represents the electron density of the crystal, while the obtained phases are attributed to lattice distortions projected onto the Bragg direction.

The typical experimental setup is shown in Fig. 2(a). A coherent X-ray beam illuminates the sample in a diamond anvil cell (DAC), where the studied crystal is aligned to the rotation center to allow the three dimensional phase retrieval. An X-ray sensitive area detector is placed at far field to catch the Bragg scattering intensity. With a phase retrieval algorithm, the reciprocal space diffraction information is Fourier transformed to the real space with multiple iterations till convergence of both amplitude and phase is reached. The amplitude is proportional to the electron density, while the phase part is used to characterize the strain field. This has been well used to construct the shape and internal strain distribution after the plastic deformation under high pressure at different pressure environment in a 400 nm sized gold particle [12]. Fig. 2(b) shows the shape and strain evolution in this nano-gold particle under pressure up to 6.4 GPa. One can see the shape evolution at various pressure which corresponds to the single crystal rheology as activated dislocations are created

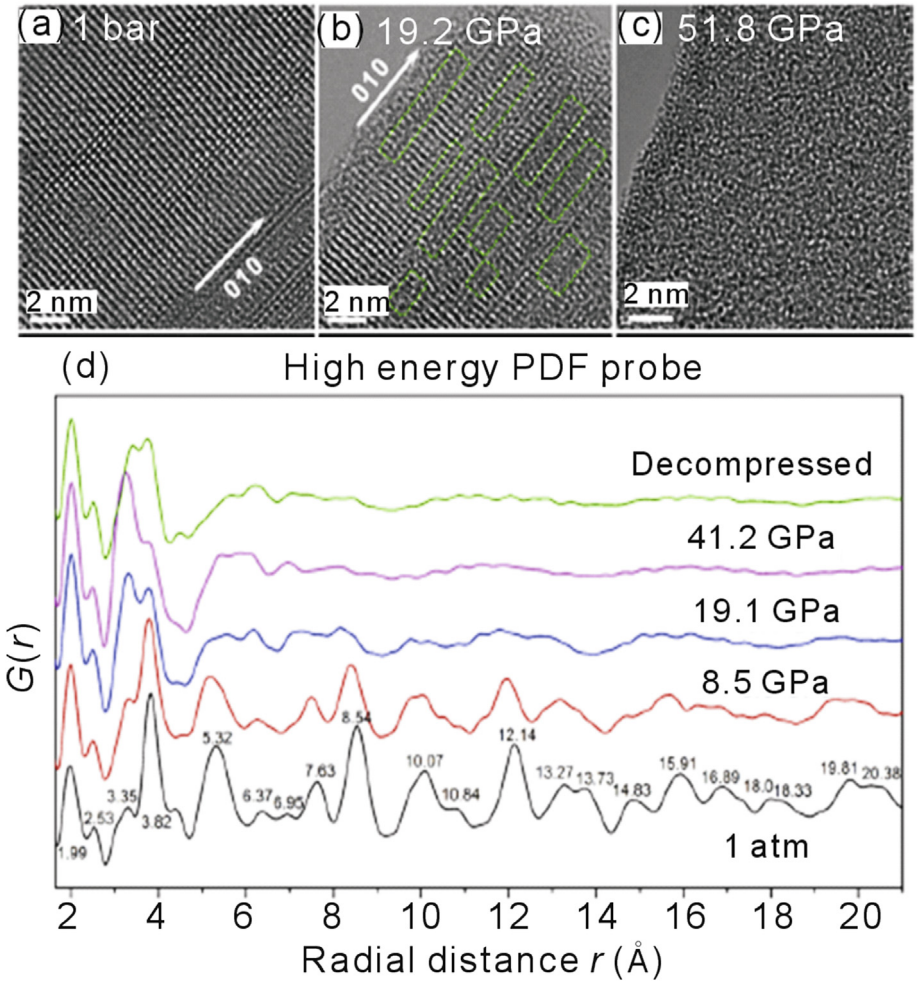

Fig. 1. Comparison of transmission electron microscopy probe on the recovered samples of Ta_2O_5 nanowire from different pressure stages and in-situ high energy PDF probe under high pressure. (a–c) are the high resolution micrographs from samples quenched from different pressures at 1 bar, 19.2 GPa and 51.8 GPa, where XRD patterns show a perfect starting single crystal structure at 1 bar, mixture with some amorphous background and partial crystal diffraction symmetry at 19.2 GPa, and total amorphized structure. (d) In-situ high energy PDF study reveals the coherent bonding distance at different pressures. Below and above 19 GPa, there is a distinguished bonding ordering length, which connects to the breakage of bonding from this pressure and up where partial and total amorphization in the sample.

and pass through the crystal; while the strain evolution gives the local lattice distortion. A continuous evolution of a nanoparticle at constant pressure has also been monitored with the CXDI method [13]. A 100 nm sized nanocrystal silver crystal under a 2.1 GPa pressure with ice VII phase serving as pressure transmitting medium. As the internal shear stress in ice VII phase is slightly above the silver strength, the activation of deformation as a function of time can be monitored with tens of namometer spatial resolution. In Fig. 2(c), the four reconstructed images shows the shape and strain distribution measured at four consequent measurements at about 15 min apart. On the third measurement, we successfully observed the twinning formation from the original nanograin.

3. Two-dimensional Van der Waals compounds

As a new dimension, high pressure can be integrated with many current, exciting new frontiers and makes major impacts. Two-dimensional (2D) materials, such as graphene, transition metal dichacogenides (TMDs), hexagonal boron nitride (h-BN), phosphorene, and silicene, possess extraordinary properties that make them promising candidates for applications in electronic, optical, semiconducting, flexible devices, bio-/nano-sensors, drug delivery, and energy storage and harvesting material. These 2D materials have covalent bonding within each monolayer to hold atoms together, while the weak van der Waals force holds the inter layers together (Fig. 3). Graphene, the 2D form of carbon atoms, has drawn much attention since 2004 when monolayer was mechanically exfoliated [2]. Suspended graphene exhibits extremely high electron mobility [14], current density [15], and thermal conductivity [16], making graphene a promising candidate for a plethora of applications in flexible electronic devices, solar cells, ultra-capacitors, spintronics, to name a few [17]. However, graphene does not exhibit a bandgap that has restricted its applications in semiconductors and optical switches where a switchable or tunable bandgap is highly desirable. From the advent of graphene [18], several 2D materials with diverse

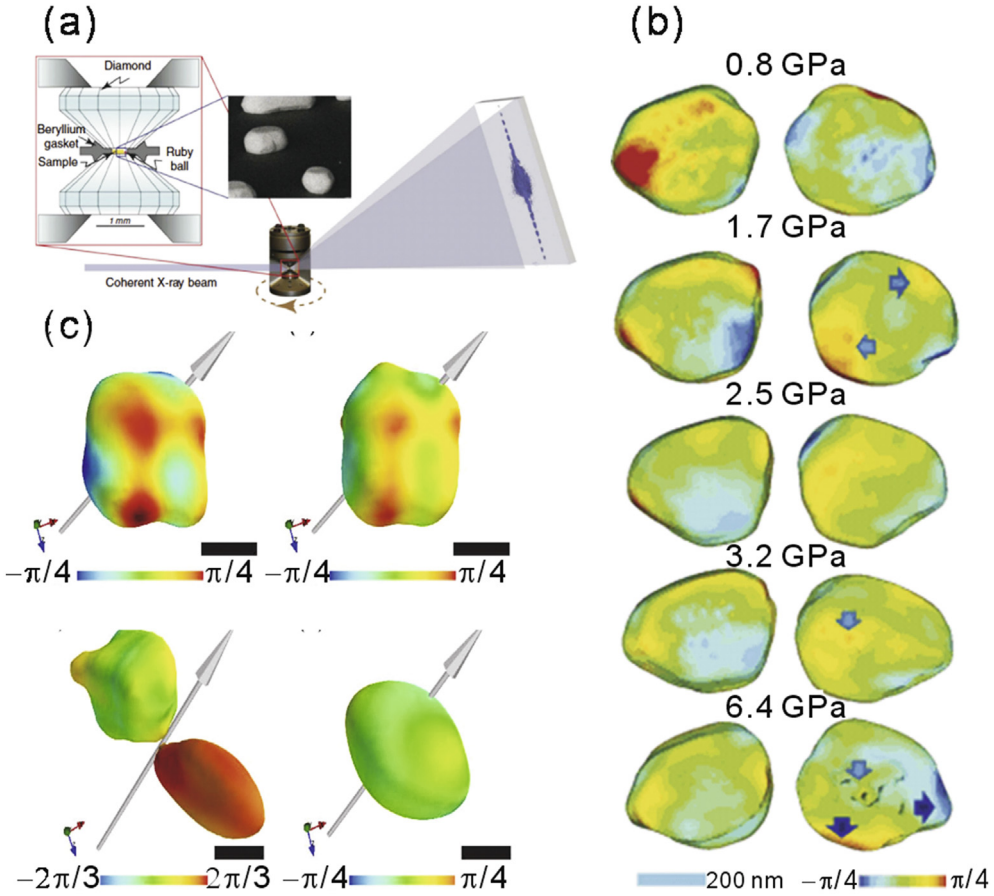

Fig. 2. (a) The typical experimental setup for a Bragg coherent X-ray diffraction imaging (CXDI). (b) The evolution of crystal shape and internal strain as a function of static pressure up to 6.4 GPa. The arrows point to the high strain location. (c) The evolution of strain and shape in a nano-cube silver crystal under a constant pressure 2.1 GPa at different time. At the third measurement, a nano-twin is observed to form with a [111] twinning direction.

bandgaps and mobilities have been discovered including insulators like h-BN [19,20], semiconductors with a bandgap such as TMDs [21] and other elemental atomic materials such as silicene and phosphorene [22,23]. In particular, TMD MX_2 compounds are formed by a layer of a transition metal atom (M: Mo, W, etc.) that are sandwiched between two layers of chalcogen atoms (X: S, Se, or Te) [21]. These layers are then bonded to each other by van der Waals force. Unlike graphene, TMDs exhibit a thickness-dependent bandgap. For example, monolayer 2H−MoS_2 has a direct gap about 2.0 eV, but bulk MoS_2 crystal possesses an indirect band-gap about 1.2 eV [24].

A tunable bandgap and high carrier mobility are among the two fundamental physical properties of the aforementioned 2D materials that are most desirable for direct applications in electronic and optical devices. Black phosphorus also known as phosphorene in the few-layer limit is also poised to be the most attractive 2D material owing to its high carrier mobility approaching that of graphene, and its thickness tunable bandgap that can be as large as that of TMDs such as MoS_2 [22,25]. Phosphorene may thus represent the much sought after high-mobility, tunable direct bandgap 2D layered crystal. However, when the number of layers in phosphorene goes down to a few layers, it becomes highly unstable and requires special protection to extend its life time making its applications rather limited. It is interesting to note that Percy Bridgman, who won the Nobel Prize in Physics in 1946 for his contributions in high-pressure physics, discovered black phosphorus in 1914 [26], but the first scientific report about monolayer and few-layer phosphorene only came out a hundred years later in 2014 [22,25].

Stacking monolayers of different species of 2D materials together produces 2D heterostructures that have demonstrated a number of unique properties arising from interlayer interactions, including modified electronic structures and bandgaps [27], spatially separated exciton [28], phonon−-phonon interactions [29], and electron charge transfer [30]. In the scheme of 3D stacking with 2D layers, individual 2D layers are integrated into a 3D heterostructure where interlayer atomic interactions could be much greater than van der Waals force. On the other hand, two or more transition metals with similar properties can be alloyed into a new layered material such as ternary 2D TMD compounds that can exhibit distinctive physical and electronic properties.

Various strategies have been adopted to tune the electronic, optical, and phononic properties of 2D compounds, including electrical gate [31], uniaxial and biaxial strain [32], magnetic field [33], temperature [34], and hydrostatic pressure. In some

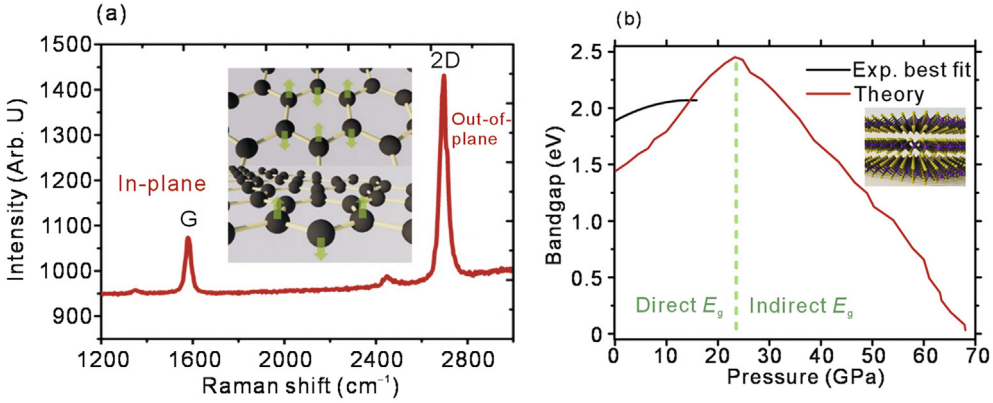

Fig. 3. (a) Structural and vibrational properties of graphene. Representative Raman spectrum of graphene showing in-plane vibration (G mode) and out-of-plane vibration (2D mode). (b) Bandgap and structure of 2H−MoS_2 [48]. Optical bandgap of 2H−MoS_2 increases in experimental observations, changes from direct to indirect, and is predicted to close at higher pressures [48].

2D materials, the electronic bandgap and lattice structure of the material is tunable by adjusting the number of layers [24,35,36], intercalation with other molecules [37–39], applied mechanical uniaxial and biaxial strain [40,41], stacked out-of-plane heterostructures [42,43], and in-plane 2D heterostructures [44,45]. Comparing with other techniques, applied compressive strain under hydrostatic pressures onto the 2D materials can drastically shorten the interlayer distance and thus significantly enhance their interlayer van der Waals interactions, which in turn can result in fine-tuned changes in their properties. Specifically, applied hydrostatic pressure in a DAC has been recently shown to induce a number of intriguing physical phenomena in 2D materials experimentally and theoretically including metallization and superconductivity in bulk TMDs, bandgap opening and direct-to-indirect bandgap transition in monolayer MoS_2 [46], strong charge transfer in hybrid graphene/MoS_2, and enhanced doping and hydrogenation in graphene [47]. In general, application of pressure modifies the van der Waals interaction between stacking layers due to rearrangement or transfer of electron charge. In particular, high-pressure DAC with a soft pressure medium can be used to apply an extremely high compressive strain of up to 30%~50% onto the 2D materials with an internal energy increase in the order of 1 eV at hydrostatic pressures up to approximately 100 GPa. In comparison, such a hydrostatic pressure extreme without inducing any damage and/or chemical impurities to the system is almost an order higher than that in the traditional uniaxial and biaxial strain devices with a strain limit of ~3%–4%. The DAC device has been coupled with *in situ* Raman spectroscopy, photoluminescence spectra, ultrafast laser spectroscopy, synchrotron X-ray spectroscopies, and electrical conductivity measurements to open up a new dimensionality for tuning the interlayer interaction to a great extent that may create a paradigm shift in our understanding of the physics of the 2D van der Waals compounds. Specifically, the strong intra-layered interactions induced by applied pressures changes our traditional prospective on the 2D materials as they are 3-dimensional connected under extreme compressive strain. A number of intriguing physics observed in previous high-pressure studies on 2D monolayers, heterostructures, and their bulk counterparts are summarized here:

3.1. Bandgap opening of monolayer TMDs

Bulk TMDs possess an indirect band-gap while monolayer TMDs can have a direct gap due to quantum confinement [24]. As shown in the analysis of the experimentally measured photoluminescence spectra, the direct bandgap of the monolayer 2H−MoS_2 increases approximately 12% from 1.8 eV at ambient conditions to 2.2 eV at ~16 GPa [48,49] (Fig. 3(b)). First-principle density function theory (DFT) calculations further show that the bandgap of 2H−MoS_2 increases with increasing pressure, changes into an indirect bandgap, and eventually closes at pressures of approximately 68 GPa. The metallization transition is also predicted to occur in bilayer, trilayer, and multilayer 2H−MoS_2 under high pressure; the metallization pressure decreases with increasing the number of layers. This metallization transition in 2H−MoS_2 is predicted to be a result of the interaction of electron-donating sulfur atoms between the van der Waals gaps. For graphene, it has been shown that ~1.0% uniaxial tensile strain on monolayers opens up a small bandgap of 100 meV [40,50,51].

3.2. Metallization and superconductivity

Applied pressures on TMDs bring the layers closer and the *c*/*a* axial ratio decreases dramatically with increasing pressure such that the interlayer interactions become much stronger. Recent experimental and theoretical studies on the pressure-dependent electronic, vibrational, optical, and structural properties of multilayered TMDs such as MoS_2 [46], WS_2 [52], $MoSe_2$ [53] reveal an electronic transition from a semiconducting-to-metallic state at high pressures. The metallization arises from the overlap of the valance band maxima and the conduction band minima at the Fermi level owing to chalcogenide atom interactions as the interlayer spacing reduces. The critical pressure for metallization is predicted to scale proportionally with film thickness in the few layer limit. The emergence of superconductivity in 2D materials has also been

reported to occur in bulk 2H–MoS_2 and black phosphorus [54] at high pressures and low temperatures. The maximum superconducting temperature T_c for bulk 2H–MoS_2 is 11.5 K at 90 GPa which is the highest T_c among TMDs.

3.3. Phonon dynamics

The phonon dynamics of the monolayer and multilayer TMDs at high pressures have been investigated using laser Raman spectroscopy [46,48,52,53]. Phonon hardening effects with pressure have been observed for both out-of-plane A_{1g} and in-plane E_{2g} modes. The in-plane E_{2g} is found to decrease in intensity with applied pressures while the out-of-plane A_{1g} is significantly enhanced. This is because the compression is more prominent along the out-of-plane *c* axis direction than the in-plane direction so the intralayer interactions are significantly enhanced at high pressures. The difference in Raman frequencies between the A_{1g} and E_{2g} modes as well as the FWHM of the Raman peaks are used to differentiate the occurrence of the metallic state from the semiconducting state. A peculiar feature observed in graphene/MoS_2 heterostructure is that A_{1g} and E_g peaks are almost identical to that of monolayer MoS_2 at high pressures, indicating that optical phonon modes in MoS_2 are not affected by enhanced interlayer charge transfer.

3.4. Charge transfer and doping

Based on theoretical and experimental investigations, charge transfer from graphene to 2H–MoS_2 has been observed to occur in monolayer graphene/MoS_2 heterostructure under hydrostatic pressures. This charge transfer causes an upward shift in the Dirac point with respect to Fermi level at high pressure leading to heavy p-type doping with a significantly enhanced carrier concentration. The estimated carrier concentration from applied pressure on the graphene/MoS_2 heterostructure is estimated to be two orders of magnitude higher than that of pristine graphene at ambient conditions. Consistent with theoretical predictions, high-pressure Raman studies of the graphene/MoS_2 heterostructure also show that the G band of graphene is strongly dependent on pressure at a rate much higher than that of the suspended graphene indicating a charge transfer from graphene to MoS_2. On the other hand, hydrogenation and chemical reaction between sp^2-bonded graphene and hydrogen have been observed to occur by heating graphene in molecular hydrogen in a high-pressure DAC at 3–5 GPa. This reaction has been suggested to promote the formation of graphene's purely sp^3-bonded analogue, graphane, potentially allowing the synthesis of other novel forms of 2D materials [47]. These aforementioned results highlight that applied hydrostatic pressure can be an effective means of achieving controllable, pressure-induced charge transfer, doping, and reaction in the 2D compounds and their heterostructures.

4. High pressure chemistry

It is well known that pressure is an important thermodynamic parameter for chemical reaction equilibrium and reaction kinetics. According to the van't Hoff equations, increasing pressure is beneficial to the reactions with negative reaction volume and will accelerate the reaction with negative activation volume. In the past, most studies are focusing on the effect of pressure on the reaction in the pressure range from several to several hundreds of MPa. The reactions are still progressing in the solution, gas phase or superfluid, which are strongly affected by diffusion and collision. In this part, we will discuss the chemistry in the range of 1–100 GPa, which will dramatically modify the electronic structure of reactants and result in novel reaction kinetics and reaction mechanisms.

The high pressure induced chemical reaction exhibits several new features: 1. The reactants tend to form more chemical bonds because of the compression of volume. 2. Diffusion of atoms is significantly suppressed if not heated up, which kinetically stabilizes the meta-stable compounds, and promotes topochemical reactions. The reaction highly depends on the local structure in the crystal of reactant, and the selectivity of the reaction will be modified dramatically. Usually the reaction with the least atom movement is most likely to proceed. 3. Applying pressure can activate the reactant molecules by forcing them to approach each other, just like applying high temperature will make more intense collisions between the molecules. The reactions will proceed when the reactant molecules overcome the energy barrier, or when pressure is released and more space for reaction is provided. In the following, we will briefly review the high pressure chemical reaction in several systems.

4.1. Ionic compound

4.1.1. Group 17

Alkaline metal halides are typical ionic compounds. Under high pressure we cannot simply understand the crystal structure and even the chemical composition using the classical chemistry. Weiwei Zhang et al. found that a series of new compounds including Na_3Cl, Na_2Cl, Na_3Cl_2, $NaCl_3$ and $NaCl_7$ are theoretically stable (Fig. 4). The orthorhombic $NaCl_3$ and two-dimensional metallic tetragonal Na_3Cl were identified by Raman spectroscopy and X-ray diffraction (XRD) in laser-heated diamond cell [55]. The polychloride Cl_3^- anion in $NaCl_3$ is similar as the well-known I_3^-, which indicates the d-orbital is evolved in the bonding. Another feature is under hundreds of GPa, Cl^- and Na^+ tend to have identical radii, which makes the non-stoichiometric packing much easier.

4.1.2. Group 15

The phase transitions of azide are well investigated due to the potential applications as energetic materials. It is predicted that the alkaline azides will polymerize to form N_6 rings and polymeric nitrogen skeletons under high pressure [56,57]. On the other hand, by controlling the decomposition of azide under high pressure, metal diazenide can be synthesized [58,59]. In this process, high pressure is critical to prevent the complete decomposition, which reminds us the significant effect of pressure on the kinetics.

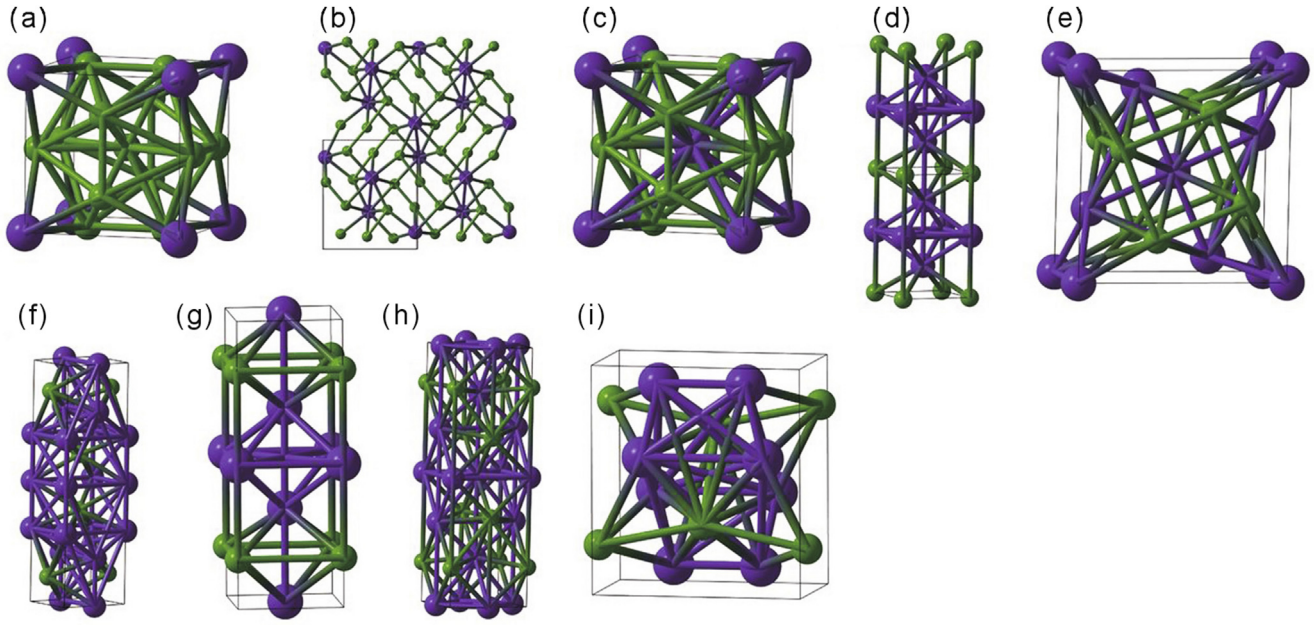

Fig. 4. Crystal structures of Na chlorides and $NaCl_7$ from Zhang et al. [55]. (a) *Pm*3-$NaCl_7$. (b) *Pnma*-$NaCl_3$. (c) *Pm*3*n*-$NaCl_3$. (d) *P*4/*mmm*-Na_3Cl. (e) *P*4/m-Na_3Cl_2. (f) *Cmmm*-Na_3Cl_2. (g) *P*4/*mmm*-Na_2Cl. (h) *Cmmm*-Na_2Cl. (i) *Imma*-Na_2Cl. Blue and green spheres denote Na and Cl atoms, respectively.

4.1.3. Group 14

The carbides show more intriguing chemistry under extreme conditions due to the bonding property of carbon. In the Ca–C system, five new compounds including Ca_5C_2, Ca_2C, Ca_3C_2, CaC and Ca_2C_3, and three polymorphs of CaC_2 including 1D chain, ribbon and 2D graphite were predicted [60,61]. Two of them (Ca_2C and Ca_2C_3) have been confirmed by in-situ XRD at the pressure up to 25 GPa and temperature up to 2000 K. In the Mg–C system, Mg_2C containing the unusual C^{4-} anion was synthesized at pressures between 15 and 30 GPa and temperatures of 1775–2275 K, and it is fully recoverable to ambient conditions [62]. Polymorphs of BeC_2 and MgC_2 containing five-membered carbon ring were predicted to be stable under high pressure [63]. BaC_2 and Li_2C_2 are found to amorphize under high pressure, probably polymerized [64,65]. A common structural feature is that the unsaturated acetylide anions tend to polymerize to decrease the volume.

Another important group of unsaturated salt, cyanide, also polymerizes upon compression. NaCN is found to amorphize and polymerize above 25 GPa according to the Raman spectroscopy. The Prussian blue compounds have a much lower amorphization pressure, around 2 GPa [66,67]. The CN^- in $K_3Fe(CN)_6$ can react with each other at pressure above 4 GPa and generate connected C=N bonds, which results in the enhancement of the electronic conductivity by ~3 orders of magnitude, to ~10^{-4} S cm^{-1} [68].

4.2. Molecular compound

4.2.1. Simple small molecular compound

Unsaturated molecules like N_2, CO_2, and O_2 will polymerize under high pressure, and most of the products will decompose when pressure is released. The bonding between the neighboring molecules will decrease the volume significantly, which is the driving force of the reaction. O_2 turns into monoclinic ε-phase at 10 GPa in which four O_2 molecules combine into a O_8 unit [69]. The molecular cluster is held together by weak chemical bonds, which was confirmed by the inelastic X-ray scattering [70].

N_2 is very inert at ambient condition and the dissociation energy is very high. Thus, the N–N single bond based polymer will release huge energy when it decomposes. At above 2000 K and above 110 GPa, the crystalline form of nonmolecular nitrogen was obtained, which is proved to be the cubic gauche structure (cg-N) [71]. CO and N_2 are isoelectronic, but the polymerization pressure is much lower [72,73]. The product is a random polymer made of lactonic entities and conjugated C=C bonds, which is an energetic material that can be recovered to ambient pressure [72].

CO_2 is another important compound with π bonds. Above 30 GPa and 1800 K, a nonmolecular phase named as CO_2–V was formed, which has a β-cristobalite structure with the space group *I-42d* [74,75]. It could quench down to 1 GPa at 300 K and convert to the molecular form at lower pressure. Another nonmolecular phase, CO_2-VI, was obtained by isothermal compression of CO_2-II above 50 GPa at 530–650 K [76]. It has a stishovite-like structure with 6-coordinated carbon atoms.

4.2.2. Complex molecular compound

Benzene (C_6H_6) starts to polymerize at 21 GPa and a white solid can be recovered to ambient pressure. This transformation was confirmed to involve an opening of benzene rings leading to a highly cross-linked polymer [77]. It turns out to be an amorphous C:H network containing both sp^2- and sp^3-bonded carbon [78]. By controlling the decompressing rate, a

crystalline one-dimensional sp^3 carbon nanomaterial can be obtained, and it is found that the polymerization proceeds through a [4 + 2] Diels–Alder cycloaddition reaction followed by intramolecular 'zipper' cascade reaction (Fig. 5) [79]. The reaction process is considered to contain the excimers produced by the charge-transfer process and the dimerization is the first stage of benzene amorphization [80]. The formation of the dimers is driven by lattice motions and the reactive contact between C atoms of nearest molecules is about 2.6 Å [81].

Acetylene is the simplest alkyne (containing C≡C bond) and the polyacetylene has very high conductivity. Due to the confined environment under high pressure, high conformation selectivity is expected. At room temperature, acetylene polymerizes at around 3.5 GPa, producing *trans*-polyacetylene dominated product [82]. At liquid nitrogen temperature, acetylene polymerizes into *cis*-polyacetylene at around 12 GPa, which transforms to *trans* when warmed up to room temperature [83]. The possible reaction path is proposed based on the crystal structure [81]. Laser may affect the polymerization product which will result in branching [84,85]. More efforts are still needed to control the reaction condition to obtain the ordered product such as the single crystal polyacetylene. Modified acetylenes can also polymerize under high pressure, but with different pressure. For example, the cyanoacetylene undergoes polymerization at pressure above 1.5 GPa [86] while phenylacetylene is above 8 GPa [87].

Different from the alkyne, the C≡N triple bond is characterized by a large dipole moment, and the arrangement of nitriles in crystals is thus affected. HCN molecules crystallize into linear chains with a head to tail alignment by strong hydrogen bonds [88]. Above 1 GPa, it polymerized into a product similar to the azulmic acid 5 [89]. The resulted amino and cyano groups indicates that the reaction involves the hydrogen migration.

4.3. High pressure chemistry reaction assisted by photochemistry

With optical excitation molecules can be exited and the molecular structure may thus be changed, which may decrease the intermolecular distance required for the chemical reaction and thus decrease the reaction pressure. The special molecular configuration may also suppress competitive reaction paths and increase the selectivity of the reaction.

The first example is about the pressure-induced polymerization of benzene in the presence of irradiation. Optical excitation decreases the reaction pressure of benzene from 23 GPa to 16 GPa without changing the product [80], indicating that the activation into an appropriate electronic state is in essence equivalent to an increase of the pressure.

Another example is about the polymerization of butadiene which shows that combining the optical excitation with pressure significantly increased the selectivity of the reaction. At 0.7 GPa, the butadiene dimerizes into vinylcyclohexene and only a trace amount of polybutadiene forms. By irradiation the high pressure sample at 488 nm, the dimerization was inhibited completely by the subsequent two-photon absorption in the 2^1A_g (S_1) state and pure *trans*-polybutadiene was obtained [90]. In the S_1 state, the molecule is stretched and the rotational barrier around the double bonds is lowered, which favors the polymerization along the molecular backbone (Fig. 6).

High pressure is a powerful method to induce and control chemical reactions, and is also a good technique to study the reaction process by pushing the molecule to approaching each other gradually. Novel materials can be obtained under extreme condition and this will be expanded further when we combined the high-pressure condition with the other reaction conditions such as the light irradiation and temperature. For example, high temperature will accelerate the diffusion, which will disturb the topochemical reaction process but helps the

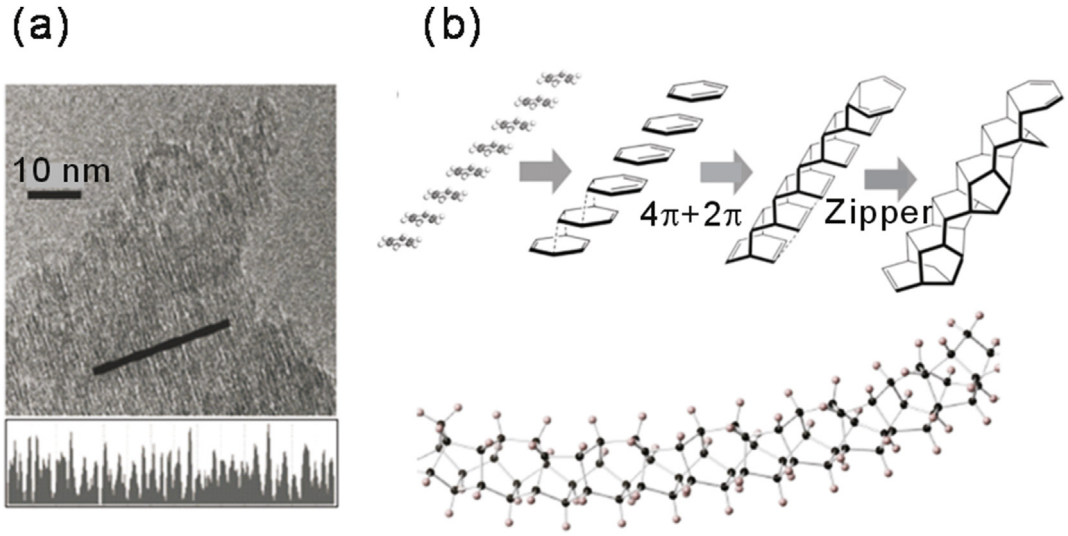

Fig. 5. The high-pressure reaction of benzene [79]. (a) Bright-field TEM micrographs of sp^3 nanothreads. (b) Nanothread formed by cycloaddition and intramolecular reaction.

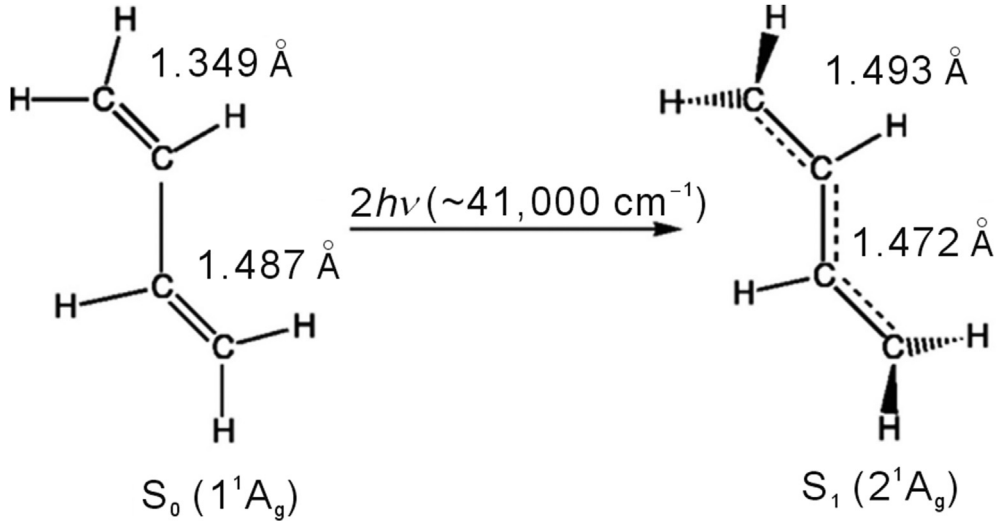

Fig. 6. Geometrical changes in the butadiene molecule induced by the S_0–S_1 two-photon electronic transition [90].

product to get crystallized. Although some interesting results have been already obtained, this area is still in the beginning stage. From the view of chemical and material synthesis, the main challenge is how the reaction under high pressure can be controlled by the experimental condition. Thus, the microscopic reaction mechanisms including the crystal structure (intermolecular distance and orientation) and the electronic structure at the threshold pressure need to be understood. In addition, the fine control of the quality of the reactant is also important because the disorder, stress and crystal defect will also affect the reaction pressure and reaction path [89].

5. Rheological study of Earth and planetary materials

Generation of high pressure and high temperature are crucial for experimental study of the Earth and planetary interior because of the extreme pressure and temperature conditions deep inside planets. While high pressure techniques described so far has enabled achieving the pressure/temperature at the center of Earth (about 360 GPa and 6000 K) using a DAC, studies of rheological properties of the Earth and planetary materials under controlled strain rate (creep experiments) have been limited to pressures nearly an order of magnitude lower than this achievable condition in a DAC (Fig. 7). Traditional stress-strain creep experiments using Paterson and Griggs apparatuses supply cylindrical stress field ($\sigma_1 = \sigma_2 \neq \sigma_3$) in gas and solid confining pressure medium respectively. However, the Paterson gas-medium apparatus [91] can only achieve a confining pressure of 0.5 GPa (equivalent to the pressure at approximately 15-km depth in the Earth) whereas the modified piston cylinder Griggs apparatus [92] with solid pressure medium is limited to a maximum pressure of 4 GPa (equivalent to approximately 135-km depth). The creep experiments using these apparatuses can be conducted under either constant stress or constant strain rate. The pressure barrier for creep experiments was broken by the development of new deformation apparatuses in conjunction with synchrotron X-ray sources [93]. D-DIA [94] and D-Tcup [95] supply cubic and octahedral stress fields respectively, which are practically approximate to cylindrical symmetry with σ_3 being independent to σ_1 and σ_2. The creep experiments with these apparatuses are mostly done with constant strain rate and the maximum pressure can reach 20 GPa in D-DIA [96] and 17 GPa in D-Tcup [95] (equivalent to the pressures in Earth's transition zone). Principally different from all these apparatuses, the rotational Drickamer apparatus (RDA) [97] supplies a combination of shear and uniaxial stresses on to a ring-shape sample. Except the complication of stress and strain geometry, RDA has advantages of higher achievable pressure and unlimited total strain

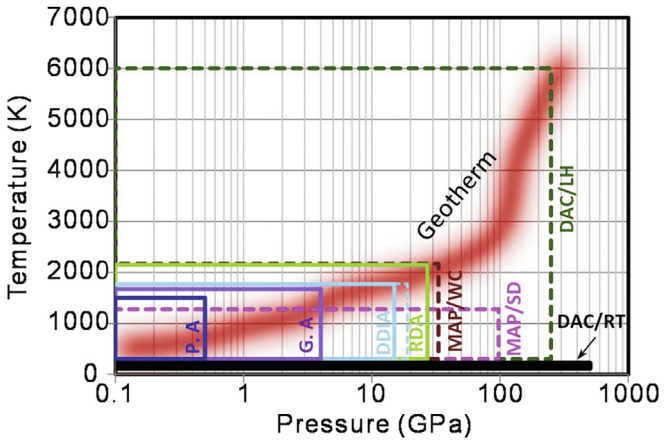

Fig. 7. Achievable pressures and temperatures in difference high pressure apparatuses. Solid lines indicate the pressure/temperature range of apparatuses capable for creep experiments; thick broken lines for regular high pressure/temperature experiments. P.A: Paterson gas-medium apparatus; G.A: Griggs solid-medium apparatus; DDIA: deformation DIA apparatus; RDA: rotational Drickamer apparatus; MAP/WC: multi-anvil press with tungsten carbide anvils; MAP/SD: multi-anvil press with sintered diamond anvils; DAC/LH: diamond anvil cell with laser heating; DAC/RT: diamond anvil cell at room temperature.

for creep experiments. A pressure of 28 GPa equivalent to that in Earth's lower mantle has been achieved recently in a RDA.

5.1. Rheological law for dislocation creep in olivine

As a dominant mineral in the upper mantle, olivine has been extensively studied for understanding the dynamics of the mantle flow. However, rheological properties of olivine are not well constrained mainly because of the difficulty in acquiring quality experimental data at high pressures. Plastic deformation in olivine occurring in the mantle proceeds mainly through migrations of crystal dislocations, i.e. dislocation creep. Under a differential stress, a dislocation propagates along a particular direction (slip direction) within a slip plane. A combination of a slip plane and slip direction defines a slip system. The strain rate for dislocation creep is described by the Orowan equation (flow law) [98]:

$$\dot{\varepsilon} = b\rho v$$

where b is the length of the Burgers vector (the unit displacement associated with a dislocation), ρ is the dislocation density (the total length of dislocations per unit volume) and v is the dislocation velocity. At high temperature, this equation becomes an exponential function [98]:

$$\dot{\varepsilon} = A\sigma^n e^{-\frac{E+PV^*}{RT}}$$

where A is a constant, σ stress, E the activation energy, V^* the activation volume for dislocation motion, R the gas constant, and the stress exponent n ranges between 3 and 5. Therefore, measuring steady state stress-strain rate relation becomes essential to establish the flow law of a mineral. Practically, the activation energy E is often determined independently to the activation volume V^* by measuring stresses and strain rates at different temperatures and a constant pressure; and the activation volume V^* is determined at different pressure and a constant temperature.

5.2. Activation energy for dislocation creep in olivine

Early experiments by Chopra and Paterson [99] using Paterson gas-medium apparatus yield an activation energy ranging from 444 kJ/mol to 498 kJ/mol for olivine (dunite) aggregate. Mei and Kohlstedt [100] later reported that this value of the activation energy is slightly higher (510 kJ/mol) in their experiments using the same apparatus. Hirth and Kohlstedt [101] conducted single crystal creep experiments and realized the easiest slip system in olivine also takes a similar activation energy, 520 kJ/mol. Experiments conducted at higher pressure (1–2 GPa) by Karato and Jung [102] using Griggs apparatus achieved a very consistent value, 510 kJ/mol, of the activation energy for olivine aggregate. All these measurements were based on directly monitoring force and position of the piston that introduces displacement to the sample. Therefore the confining pressure is low. Application of high energy synchrotron X-rays that can penetrate solid-medium without interference with pressure generation to measure sample stress and strain remarkably increase the confining pressure for creep experiments. New measurements were conducted at pressures up to 9.6 GPa using RDA by Kawazoe et al. [103] and D-DIA by Durham et al. [104] and Li et al. [105]. With reference to the previous low pressure data, they inferred the activation energy to 530, 500 and 470 kJ/mol respectively. Up to date, majority of the measurements with different experimental techniques indicate that the activation energy of dislocation creep in olivine aggregate lies in a range of 450–530 kJ/mol. Distinctly lower values of 104–112 kJ/mol and 133 kJ/mol were obtained in high pressure (3–8 GPa) D-DIA experiments using forsterite single crystals by Raterron et al. [106] and using polycrystalline San Carlos olivine by Hilairet et al. [107] respectively. Raterron et al. [106] attribute the low activation energy to pressure-induced dislocation cross-slip mechanism. Karato [108] argued that the Peierls mechanism rather than power-law creep may be responsible for such low activation energy values. Further investigations are needed to clarify this anomaly in experimental results.

5.3. Activation volume for dislocation creep in olivine

Compared to the results of activation energy, experimental values of the activation volume for dislocation creep in olivine are much more diverse, ranging from 0 to 27 cm^3/mol. The early experiment using Griggs apparatus by Ross et al. [109] indicated an activation volume of 13.4 cm^3/mol in the pressure range of 0.5–1.5 GPa. Green and Borch [110] later modified the value to 27 cm^3/mol based on their data from 0.6 to 2.0 GPa. Karato and Jung [102] restated that it is more reasonable to consider 14 cm^3/mol to be activation volume according to their experiment using the same type of apparatus (0.3–2.0 GPa). On the other hand, based on the study of silicon or oxygen diffusion in olivine as a function of pressure (5–10 GPa), Béjina et al. [111] reported that the activation volume of olivine is close to 0 cm^3/mol. Subsequent creep experiments at high pressures up to 8 GPa using D-DIA by Li et al. [105] (on polycrystalline olivine) and by Raterron et al. [106] (on forsterite single crystal) confirmed this low activation volume value (<5 cm^3/mol). However, in later experiments using the same instrument, Durham et al. [104] showed that the activation volume can be as high as 9.5 cm^3/mol from their polycrystalline experiment in the pressure range of 2.7–4.9 GPa; and Raterron et al. [112] reported that the activation volume for the easy slip systems [100](010) and [100](001) is 12 cm^3/mol according to their olivine single crystal creep experiment at 3.5–8.5 GPa. In a RDA creep experiment from 4.9 to 9.6 GPa, Kawazoe et al. [103] claimed that their creep data may yield an activation volume between 15 cm^3/mol and 20 cm^3/mol. Accounting for the result from recovered experiments, 6 cm^3/mol from Karato et al. [113] (up to 10 GPa), 11 cm^3/mol from Kohlstedt et al. [114] at 0.5 GPa (or 19 cm^3/mol corrected by Karato [115]), and 14 cm^3/mol from Karato and Ogawa [116] (up to 2 GPa) and Karato and Rubie [117] (0.3–15 GPa), the experimental results for the

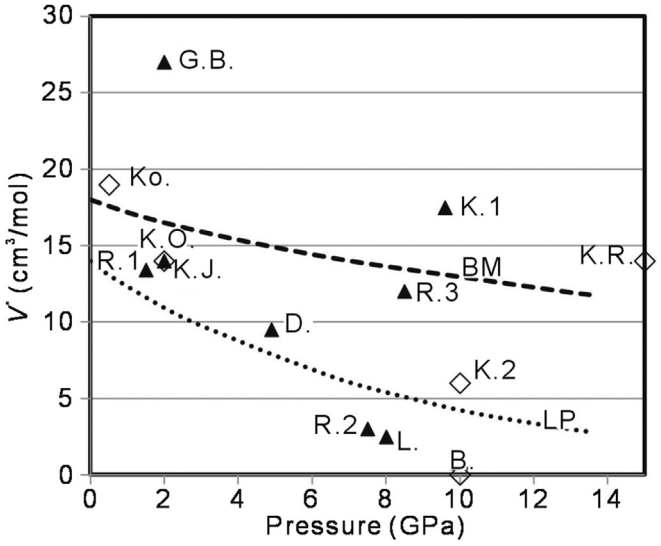

Fig. 8. Experimental values of the activation volume of dislocation creep in olivine measured in different pressure range. The data are plotted at the upper end of the pressure range. Solid symbols are from creep experiments, R.1: Ross et al. (1979) [109]; G.B: Green and Borch (1987) [110]; K.J.: Karato and Jung (2003) [102]; R.2: Raterron et al. (2007) [106]; L.: Li et al. (2006) [105]; D.: Durham et al. (2009) [104]; R.3: Raterron et al. (2009) [112]; K.1: Kawazoe et al. (2009) [103]. Open symbols are from recovered experiments, B.: Béjina et al. (1997) [111]; K.2: Karato et al. (1993) [113]; Ko.: Kohlstedt et al. (1980) [114]; K.O.: Karato and Ogawa (1982) [116]; K.R.: Karato and Rubie (1997) [117] Broken line indicates the calculated estimation of pressure effect based on the change of bulk modulus along the mantle geotherm; dotted line indicates that based on the change of the liquidus of peridotite with pressure by Hirth and Kohlstedt [101].

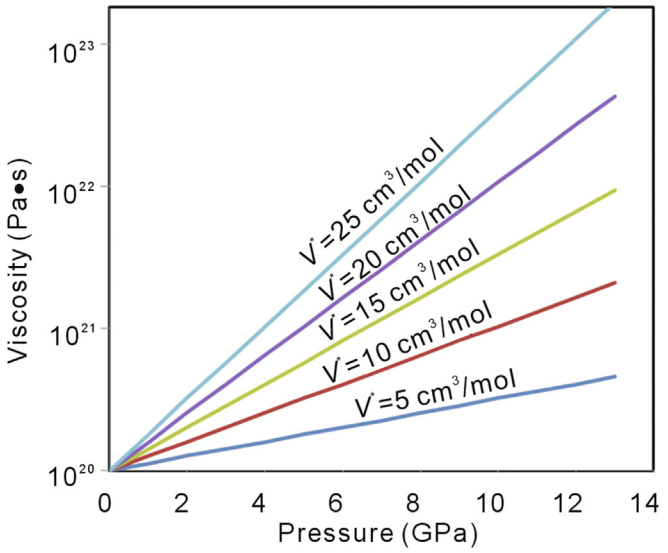

Fig. 9. Projected viscosity as a function of pressure for different activation volumes of dislocation creep as indicated. Viscosity at ambient pressure is assumed to be 1×10^{20} Pa · s. Viscosities are calculated with stress exponent $n = 3.5$ and $T = 1473$ K.

activation volume of dislocation creep in olivine scatter all over from 0 to 27 cm^3/mol. Green and Borch [110] suggested that the activation volume may vary as a function of pressure. Fig. 8 shows a summary of the experimental results of measured activation volumes together with calculated estimates of the pressure effect based on the change of bulk modulus along the mantle geotherm and the change of the liquidus of peridotite with pressure by Hirth and Kohlstedt [101]. The trend of change in the viscosity as a function of pressure is quite divergent. As shown in Fig. 9, when the activation energy changes from 5 cm^3/mol to 25 cm^3/mol, the expected viscosity may differ nearly 3 orders of magnitude at the pressure equivalent to that at bottom of the upper mantle.

Significant advances in technological development for the study of rheological properties of Earth and planetary materials have been made. Increase of the achievable pressure for creep experiments enables us to expand the research from the Earth's crust conditions to deep mantle. Nevertheless, refinements of the technique to improve the reliability of experimental data are still indispensable in order to comprehend accurately the Earth and planetary interiors.

6. Deformation under extreme environments

Extreme environments usually give rise to the special modifications in the properties of materials. In this section, we mainly review the deformation of materials under high pressure compression. We focus on the plastic deformation of nanomaterials and Earth materials because a great amount of significant work were reported in last decade. Ramp compression can generate atomic pressure and involve the contribution of inner-shell electrons, possibly opening up the new chapters of physics. Some ramp work is highlighted although not much deformation studies with the ramp compression method are available.

6.1. Plastic deformation of nanomaterials

Understanding the plastic deformation of nanocrystalline materials is a longstanding challenge. Variously controversial observations have been reported. Post-deformation analysis of compressed or indented nanocrystalline nickel does not indicate major dislocation debris [118], whereas dislocations are observed in 10 nm nickel and 9 nm platinum particles [9,119]. Deformation twinning and disclination have also been observed on nanocrystals [120–123]. Although it is commonly believed that the intrinsic deformation behaviors of nanomaterials arise from the interplay between defects and grain-boundary (GB) processes [123,124], the precise trade-offs between these deformation mechanisms are still unclear. It has been proposed that below a critical length scale the strength of nanometals would exhibit a reverse Hall-Petch size dependence because in the plastic deformation of fine nanocrystals, dislocation activity gives way to grain boundary sliding, diffusion, and grain rotation [125,126]. In contrast, twin thickness has been found to affect the maximum strength of copper, implying that the plastic deformation of nanomaterials is not necessarily related to GB-mediated processes [122]. Indeed, it has been proposed that dislocation nucleation governs material softening in nano-twinned metals [121].

For a long time, *in situ* observation of plastic deformation in ultrafine nanocrystals has been difficult, precluding the direct exploration of mechanics at nanometer scales. With the radial diamond-anvil cell (rDAC) X-ray diffraction technique, which is a relatively recently developed technique for geophysical research, Chen and co-workers have plastically deformed nickel particles of 500, 20 and 3 nm diameter to pressure above 35 GPa [127] and observe *in situ* the texture development during plastic deformation (Fig. 10). Significant texturing is observed at pressures above 18.5 GPa for 3 nm nickel, indicating that under high external pressures, dislocation activities can be extended down to a few-nanometer length scale. The size of nanocrystals has long been viewed as providing a limit on dislocation activity and associated deformation. Dislocation-mediated plastic deformation and texturing are expected to become inactive below a critical particle size, which is often thought to be between 10 and 30 nm based on computer simulations [126] and TEM analysis [128]. The new finding in ultrafine nickel [127] is at odds with the conventional belief that dislocation activities stop below ~10 nm or even larger particle sizes.

Over many decades, dislocations have never been considered as the main plastic deformation mechanisms of ceramics at low temperature. According to classical theories [129], ceramics are brittle mainly because dislocation activity is suppressed by cracking, whereas it is believed that nanoceramicsmay exhibit improved ductility due to greatly increased diffusivities [130]. The *in situ* texturing and TEM observations of stressed bulk- and nano-sized spinel ceramics indicate that dislocation activities become operative in nanoceramics. This new finding adds new knowledge on the deformation of materials: the role of dislocations cannot be ignored in nanoceramics.

6.2. Plastic deformation of Earth materials

The geological processes such as plate tectonics and mantle convection involve the plastic deformation of Earth materials, therefore understanding the plastic deformation of minerals and rocks are the important part of research work on Earth science [131]. Because of the relatively low pressure and temperature of the Earth's crust, the rheological properties of crustal materials are more accessible than those of the materials of the core and mantle. For the plastic deformation of Earth materials under extreme condition, here we mainly talk about the Earth's core and mantles.

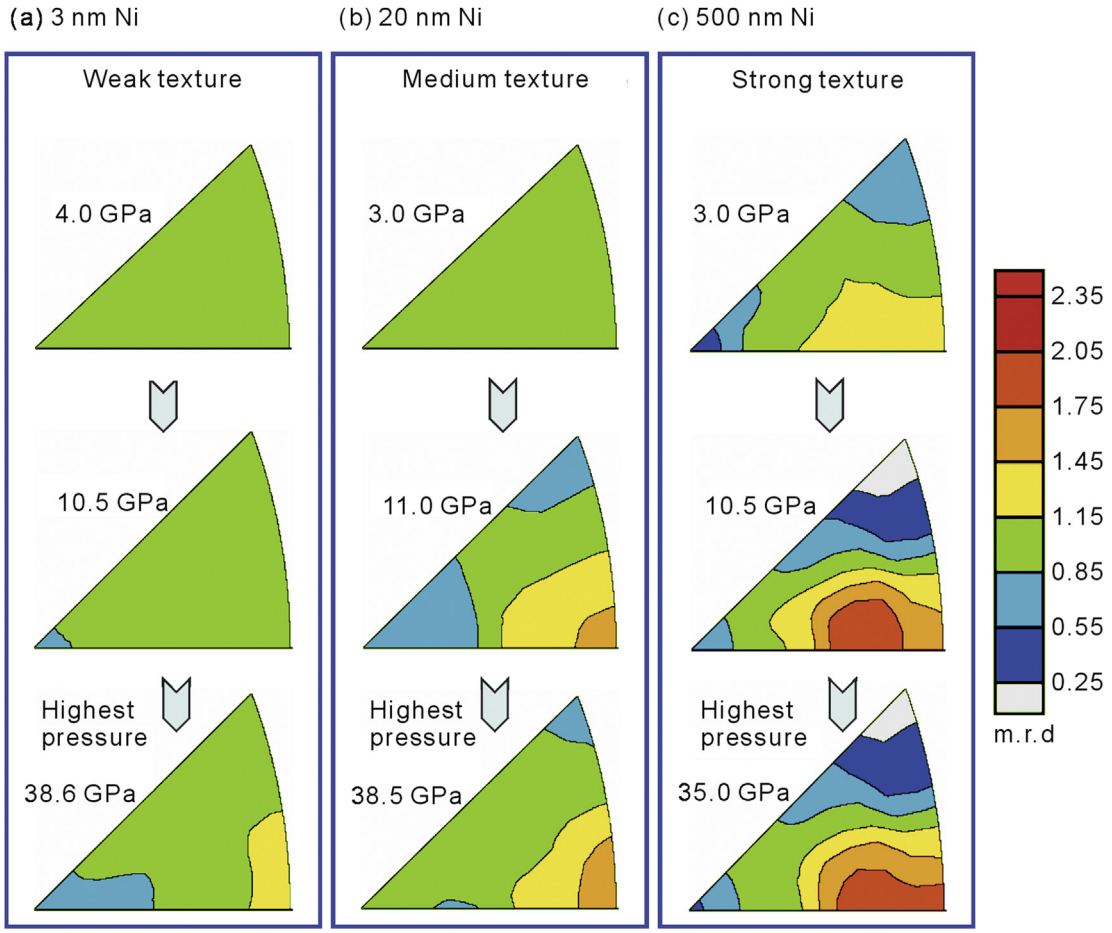

Fig. 10. Inverse pole figures of 3 nm (a), 20 nm (b), and 500 nm (c) nickel along the compression direction (normal direction). Equal area projection and a linear scale are used. The degree of lattice preferred orientation (texture strength) is expressed as multiples of random distribution (m.r.d.), where m.r.d. = 1 denotes random distribution and a higher m.r.d. number represents stronger texture [127].

The Earth core is mainly made of iron and small concentration of light elements. The outer core is thought to be made of liquid and so its deformation does not play an important role in the core dynamics. The inner core is solid iron or iron-rich alloy possibly with a hexagonal close packed structure [132]. The seismic anisotropy and seismic wave attenuation suggest that dislocations creep is the possible deformation mechanisms of the inner core [133–136]. Some attempts have been made to measure the deformation of hcp iron at high pressure and high temperature condition [137,138], however, meaningful relevance still demands the deformation investigation made at the real pressure and temperature condition of the Earth core.

Because of the huge volume, the Earth's mantle plays an important role in the dynamics and evolution of the planet. The lower mantle of Earth is composed mainly of (Mg,Fe)SiO_3 perovskite and (Mg,Fe)O. Miyagi and co-workers found that when $MgSiO_3$ post-perovskite is compressed from 148 to 185 GPa, the preferred orientation associated with slip plane (001) is more than doubles in strength [139]. This contrasts with a previous experiment that recorded preferred orientation likely generated during the phase transformation rather than deformation. The plastic deformation experiments of polycrystalline $MgGeO_3$ post-perovskite at pressures up to 130 GPa suggest (010) as a slip plane [140]. The lattice planes near (100) become aligned perpendicular to the compression direction, suggesting that slip on (100) or (110) dominated plastic deformation. A numerical model of seismic anisotropy in the D″ region implies a maximum contribution of post-perovskite to shear wave splitting of 3.7% with an oblique polarization. The transition zone of Earth's mantle is made mainly of high-pressure polymorphs of olivine and pyroxenes. Dislocation creep is thought to be the main deformation mechanism [141], however, Karato et al. [142] reported the evidence for dislocation-diffusional creep in ringwoodite. Diffusional creeps seem to be favored in the fine-grained samples. The effect of water on the deformation of these minerals has attracted some interests but there is still no consensus on it [143,144].

6.3. Shockless compression of materials

Achieving the cool dense states of matter with high energy density, applicable to planetary interiors, for example, has been long experimentally difficult. In recent years, a technique named ramp compression emerged for this purpose [145–147]. By sending a laser-induced shock wave through a pre-compressed sample inside a diamond-anvil cell, pressures to the 10- to 100-TPa can be achieved. Such investigations provide the knowledge that is relevant to planetary science, testing first-principles theories of condensed matter, and experimentally studying a new regime of chemical bonding. Admittedly, in-situ probing of materials properties during ramp compression is still limited. For instances, the deformation investigations of ramp compressed materials are very rare, leaving great spaces for future exploration. Here we introduce several representative pieces of work although they are not much specifically relevant to the deformation studies.

In the ramp compression of water, Lee and co-workers observed the onset of opacity followed by enhanced reflectivity in the initially transparent water [148]. The onset of reflectivity at infrared wavelengths can be interpreted as a semiconductor↔electronic conductor transition in water, indicating that conductivity in the deep interior of “icy” giant planets is greater than realized previously because of an additional contribution from electrons.

By applying laser-driven shocks to statically compressed helium, EOS data have been obtained with sufficient accuracy to test theoretical predictions [149]. Tuning the pre-compression before shock loading enables the measurement of a family of Hugoniots, which can test EOS models over a broader range than the principal Hugoniot alone, and can separate the effects of temperature and density on the EOS. The SCVH model used for astrophysical applications is found to agree well with the experimental data. In a following ramp compression experiment, P. M. Ceiller et al. observed the insulator-to-conducting transition in dense fluid helium [150]. This work provides a benchmark to test the models that describe helium ionization at conditions found in astrophysical objects, such as cold white dwarf atmospheres.

In the laser-driven ramp compression on hydrogen and deuterium [151], the observations of shock velocity and thermal emission provide complete equation of state data (pressure, density, internal energy, and temperature) in the dense fluid regime up to 175 GPa. Specific heat and Grüneisen coefficient are calculated directly from the data and compared to theory. It is found that the continuous transition from an electrically insulating to conducting fluid state is increasingly sensitive to temperature with increasing density. In a recent report on a ramp compression of deuterium [152], Knudson et al. presented the direct observation of an abrupt insulator-to-metal transition in dense liquid deuterium, well advancing the work of the metallization of hydrogen.

7. Conclusion

The above examples show the universal impact of pressure to a broad spectrum of multidisciplinary physical sciences. To fundamental physics and chemistry, pressure provides a powerful and extensive knob for simultaneously tuning all structural, electronic, magnetic, optical and elastic properties, thus providing critical tests for hypotheses and theories relating these properties. Pressure can greatly enhance the studies of newly emerged topics such as the examples of 2D materials. Pressure is also used for discoveries of novel phenomena, and for breakthroughs of new records. For instance, the recent news of record high superconducting temperature of 203 K in high-pressure hydrogen sulfide [153] has led to great excitement among the superconductor research community. To materials science, the extremely useful properties, such as materials of ultrahigh hardness [154,155], at high pressures can often be preserved (quenched) to ambient conditions for applications. Even when it is not quenchable, the knowledge

garnered at high pressures can often be used for room pressure synthesis with alternative chemistry. For Earth and planetary sciences, the vast majority parts of these bodies are in their deep interiors under high pressures. High-pressure research is essential for understanding their internal structures and processes. With the rapid development and integration of high-pressure tools, we may expect major booms in all these frontiers at high pressures that lead to advances in each individual discipline.

Acknowledgments

The authors acknowledge the support of NSAF Grant No. U1530402.

References

[1]. L. Dubrovinsky, N. Dubrovinskaia, E. Bykova, M. Bykov, V. Prakapenka, C. Prescher, K. Glazyrin, H.-P. Liermann, M. Hanfland, M. Ekholm, Q. Feng, L.V. Pourovskii, M.I. Katsnelson, J.M. Wills, I.A. Abrikosov, The most incompressible metal osmium at static pressures above 750 gigapascals, Nature 525 (2015) 226−229.

[2]. K.S. Novoselov, A.K. Geim, S. Morozov, D. Jiang, Y. Zhang, Sa Dubonos, I. Grigorieva, A. Firsov, Electric field effect in atomically thin carbon films, Science 306 (2004) 666−669.

[3]. L. Wang, Y. Ding, W. Yang, W. Liu, Z. Cai, J. Kung, J. Shu, R.J. Hemley, W.L. Mao, H.K. Mao, Nanoprobe measurements of materials at megabar pressures, Proc. Nat. Acad. Sci. USA 107 (2010) 6140−6145.

[4]. Y. Ding, J. Fernandez-Rodriguez, J. Kim, F. Li, D. Casa, M. Upton, T. Gog, H.K. Mao, M. van Veenendaal, Spin-ordering mediated orbital hybridization in CoO at high pressures, Phys. Rev. B 86 (2012) 094107.

[5]. D. Haskel, G. Fabbris, M. Zhernenkov, P.P. Kong, C.Q. Jin, G. Cao, M. van Veenendaal, Pressure tuning of the spin-orbit coupled ground state in Sr_2IrO_4, Phys. Rev. Lett. 109 (2012) 027204.

[6]. Y.Q. Cai, D.S. Coburn, A. Cunsolo, J.W. Keister, M.G. Honnicke, X.R. Huang, C.N. Kodituwakku, Y. Stetsko, A. Suvorov, N. Hiraoka, K.D. Tsuei, H.C. Wille, The ultrahigh resolution IXS Beamline of NSLS-II: recent advances and scientific opportunities, J. Phys. Conf. Ser. 425 (2013) 202001.

[7]. J. Miao, T. Ishikawa, I.K. Robinson, M.M. Murnane, Beyond crystallography: diffractive imaging using coherent X-ray light sources, Science 348 (2015) 530−535.

[8]. L. Ehm, S.M. Antao, J. Chen, D.R. Locke, F.M. Michel, C.D. Martin, T. Yu, J.B. Parise, P.L. Lee, P.J. Chupas, S.D. Shastri, Q. Guo, Studies of local and intermediate range structure in crystalline and amorphous materials at high pressure using high-energy X-rays, Powder Diffr. 22 (2007) 108−112.

[9]. L. Wang, W. Yang, Y. Ding, Y. Ren, S. Xiao, B. Liu, S.V. Sinogeikin, Y. Meng, D.J. Gosztola, G. Shen, R.J. Hemley, W.L. Mao, H.K. Mao, Size-dependent amorphization of nanoscale Y_2O_3 at high pressure, Phys. Rev. Lett. 105 (2010) 095701.

[10]. X. Lü, Q. Hu, W. Yang, L. Bai, H. Sheng, L. Wang, F. Huang, J. Wen, D.J. Miller, Y. Zhao, Pressure-induced amorphization in single crystal Ta_2O_5 nanowires: a kinetic mechanism and improved electrical conductivity, J. Am. Chem. Soc. 135 (2013) 13947−13953.

[11]. M.A. Pfeifer, G.J. Williams, I.A. Vartanyants, R. Harder, I.K. Robinson, Three-dimensional mapping of a deformation field inside a nanocrystal, Nature 442 (2006) 63−66.

[12]. W. Yang, X. Huang, R. Harder, J.N. Clark, I.K. Robinson, H.K. Mao, Coherent diffraction imaging of nanoscale strain evolution in a single crystal under high pressure, Nat. Commun. 4 (2013) 1680.

[13]. X. Huang, W. Yang, R. Harder, Y. Sun, Y. Ming Lu, S. Chu, I.K. Robinson, H.K. Mao, Deformation twinning of a silver nanocrystal under high pressure, Nano Lett. 15 (2015) 7644−7649.

[14]. A.S. Mayorov, R.V. Gorbachev, S.V. Morozov, L. Britnell, R. Jalil, L.A. Ponomarenko, P. Blake, K.S. Novoselov, K. Watanabe, T. Taniguchi, Micrometer-scale ballistic transport in encapsulated graphene at room temperature, Nano Lett. 11 (2011) 2396−2399.

[15]. J.H. Seol, I. Jo, A.L. Moore, L. Lindsay, Z.H. Aitken, M.T. Pettes, X. Li, Z. Yao, R. Huang, D. Broido, Two-dimensional phonon transport in supported graphene, Science 328 (2010) 213−216.

[16]. A.A. Balandin, S. Ghosh, W. Bao, I. Calizo, D. Teweldebrhan, F. Miao, C.N. Lau, Superior thermal conductivity of single-layer graphene, Nano Lett. 8 (2008) 902−907.

[17]. F. Bonaccorso, Z. Sun, T. Hasan, A. Ferrari, Graphene photonics and optoelectronics, Nat. Photonics 4 (2010) 611−622.

[18]. A.K. Geim, K.S. Novoselov, The rise of graphene, Nat. Mater. 6 (2007) 183−191.

[19]. J. Lee, T.-J. Ha, K.N. Parrish, S.F. Chowdhury, L. Tao, A. Dodabalapur, D. Akinwande, High-performance current saturating graphene field-effect transistor with hexagonal boron nitride dielectric on flexible polymeric substrates, Electron Device Lett. IEEE 34 (2013) 172−174.

[20]. I. Meric, C.R. Dean, N. Petrone, W. Lei, J. Hone, P. Kim, K.L. Shepard, Graphene field-effect transistors based on boron nitride dielectrics, Proc. IEEE 101 (2013) 1609−1619.

[21]. Q.H. Wang, K. Kalantar-Zadeh, A. Kis, J.N. Coleman, M.S. Strano, Electronics and optoelectronics of two-dimensional transition metal dichalcogenides, Nat. Nano 7 (2012) 699−712.

[22]. L. Li, Y. Yu, G.J. Ye, Q. Ge, X. Ou, H. Wu, D. Feng, X.H. Chen, Y. Zhang, Black phosphorus field-effect transistors, Nat. Nano 9 (2014) 372−377.

[23]. L. Tao, E. Cinquanta, D. Chiappe, C. Grazianetti, M. Fanciulli, M. Dubey, A. Molle, D. Akinwande, Silicene field-effect transistors operating at room temperature, Nat. Nano 10 (2015) 227−231.

[24]. A. Splendiani, L. Sun, Y. Zhang, T. Li, J. Kim, C.-Y. Chim, G. Galli, F. Wang, Emerging photoluminescence in monolayer MoS_2, Nano Lett. 10 (2010) 1271−1275.

[25]. H. Liu, A.T. Neal, Z. Zhu, Z. Luo, X. Xu, D. Tománek, P.D. Ye, Phosphorene: an unexplored 2D semiconductor with a high hole mobility, ACS Nano 8 (2014) 4033−4041.

[26]. P.W. Bridgman, Two new modifications of phosphorus, J. Am. Chem. Soc. 36 (1914) 1344−1363.

[27]. Y. Zhang, T.-T. Tang, C. Girit, Z. Hao, M.C. Martin, A. Zettl, M.F. Crommie, Y.R. Shen, F. Wang, Direct observation of a widely tunable bandgap in bilayer graphene, Nature 459 (2009) 820−823.

[28]. F. Ceballos, M.Z. Bellus, H.-Y. Chiu, H. Zhao, Ultrafast charge separation and indirect exciton formation in a MoS_2−$MoSe_2$ van der Waals heterostructure, ACS Nano 8 (2014) 12717−12724.

[29]. D. Boschetto, L. Malard, C.H. Lui, K.F. Mak, Z. Li, H. Yan, T.F. Heinz, Real-time observation of interlayer vibrations in bilayer and few-layer graphene, Nano Lett. 13 (2013) 4620−4623.

[30]. X. Hong, J. Kim, S.-F. Shi, Y. Zhang, C. Jin, Y. Sun, S. Tongay, J. Wu, Y. Zhang, F. Wang, Ultrafast charge transfer in atomically thin MoS_2/WS_2 heterostructures, Nat. Nano 9 (2014) 682−686.

[31]. B. Radisavljevic, A. Radenovic, J. Brivio, V. Giacometti, A. Kis, Single-layer MoS_2 transistors, Nat. Nano 6 (2011) 147−150.

[32]. W.S. Yun, S. Han, S.C. Hong, I.G. Kim, J. Lee, Thickness and strain effects on electronic structures of transition metal dichalcogenides: 2H-MX_2 semiconductors (M = Mo, W; X = S, Se, Te), Phys. Rev. B 85 (2012) 033305.

[33]. H. Cao, G. Aivazian, Z. Fei, J. Ross, D.H. Cobden, X. Xu, Photo-Nernst Current in Graphene, arXiv Preprint arXiv:1510.00765, 2015.

[34]. S. El-Mahalawy, B. Evans, Temperature dependence of the electrical conductivity and hall coefficient in 2H-MoS_2, $MoSe_2$, WSe_2, and $MoTe_2$, Phys. Status Solidi (B) 79 (1977) 713−722.

[35]. A. Berkdemir, H.R. Gutierrez, A.R. Botello-Mendez, N. Perea-Lopez, A.L. Elias, C.-I. Chia, B. Wang, V.H. Crespi, F. Lopez-Urias, J.-C. Charlier, H. Terrones, M. Terrones, Identification of individual and few layers of WS_2 using Raman spectroscopy, Sci. Rep. 3 (2013).

[36]. R. Ganatra, Q. Zhang, Few-layer MoS_2: a promising layered semiconductor, ACS Nano 8 (2014) 4074−4099.

[37]. M.S. Dresselhaus, Intercalation in layered materials, MRS Bull. 12 (1987) 24−28.

[38]. B. Mahler, V. Hoepfner, K. Liao, G.A. Ozin, Colloidal synthesis of 1T-WS_2 and 2H-WS_2 nanosheets: applications for photocatalytic hydrogen evolution, J. Am. Chem. Soc. 136 (2014) 14121–14127.
[39]. F.S. Ohuchi, W. Jaegermann, C. Pettenkofer, B.A. Parkinson, Semiconductor to metal transition of WS_2 induced by K intercalation in ultrahigh vacuum, Langmuir 5 (1989) 439–442.
[40]. Z.H. Ni, T. Yu, Y.H. Lu, Y.Y. Wang, Y.P. Feng, Z.X. Shen, Uniaxial strain on graphene: Raman spectroscopy study and band-gap opening, ACS Nano 2 (2008) 2301–2305.
[41]. H.J. Conley, B. Wang, J.I. Ziegler, R.F. Haglund, S.T. Pantelides, K.I. Bolotin, Bandgap engineering of strained monolayer and bilayer MoS_2, Nano Lett. 13 (2013) 3626–3630.
[42]. G.S. Duesberg, Heterojunctions in 2D semiconductors: a perfect match, Nat. Mater. 13 (2014) 1075–1076.
[43]. A.K. Geim, I.V. Grigorieva, Van der Waals heterostructures, Nature 499 (2013) 419–425.
[44]. L. Ci, L. Song, C. Jin, D. Jariwala, D. Wu, Y. Li, A. Srivastava, Z.F. Wang, K. Storr, L. Balicas, F. Liu, P.M. Ajayan, Atomic layers of hybridized boron nitride and graphene domains, Nat. Mater. 9 (2010) 430–435.
[45]. Y. Gong, J. Lin, X. Wang, G. Shi, S. Lei, Z. Lin, X. Zou, G. Ye, R. Vajtai, B.I. Yakobson, H. Terrones, M. Terrones, Beng K. Tay, J. Lou, S.T. Pantelides, Z. Liu, W. Zhou, P.M. Ajayan, Vertical and in-plane heterostructures from WS_2/MoS_2 monolayers, Nat. Mater. 13 (2014) 1135–1142.
[46]. A.P. Nayak, S. Bhattacharyya, J. Zhu, J. Liu, X. Wu, T. Pandey, C. Jin, A.K. Singh, D. Akinwande, J.-F. Lin, Pressure-induced semiconducting to metallic transition in multilayered molybdenum disulphide, Nat. Commun. 5 (2014) 3731.
[47]. D. Smith, R.T. Howie, I.F. Crowe, C.L. Simionescu, C. Muryn, V. Vishnyakov, K.S. Novoselov, Y.-J. Kim, M.P. Halsall, E. Gregoryanz, J.E. Proctor, Hydrogenation of graphene by reaction at high pressure and high temperature, ACS Nano 9 (2015) 8279–8283.
[48]. A.P. Nayak, T. Pandey, D. Voiry, J. Liu, S.T. Moran, A. Sharma, C. Tan, C.-H. Chen, L.-J. Li, M. Chhowalla, Pressure-dependent optical and vibrational properties of monolayer molybdenum disulfide, Nano Lett. 15 (2014) 346–353.
[49]. X. Dou, K. Ding, D. Jiang, B. Sun, Tuning and identification of interband transitions in monolayer and bilayer molybdenum disulfide using hydrostatic pressure, ACS Nano 8 (2014) 7458–7464.
[50]. J. Nicolle, D. Machon, P. Poncharal, O. Pierre-Louis, A. San-Miguel, Pressure-mediated doping in graphene, Nano Lett. 11 (2011) 3564–3568.
[51]. J.E. Proctor, E. Gregoryanz, K.S. Novoselov, M. Lotya, J.N. Coleman, M.P. Halsall, High-pressure Raman spectroscopy of graphene, Phys. Rev. B 80 (2009) 073408.
[52]. A.P. Nayak, Z. Yuan, B. Cao, J. Liu, J. Wu, S.T. Moran, T. Li, D. Akinwande, C. Jin, J.-F. Lin, Pressure-modulated conductivity, carrier density, and mobility of multilayered tungsten disulfide, ACS Nano 9 (2015) 9117–9123.
[53]. Z. Zhao, H. Zhang, H. Yuan, S. Wang, Y. Lin, Q. Zeng, G. Xu, Z. Liu, G.K. Solanki, K.D. Patel, Y. Cui, H.Y. Hwang, W.L. Mao, Pressure induced metallization with absence of structural transition in layered molybdenum diselenide, Nat. Commun. 6 (2015) 7312.
[54]. I. Shirotani, J. Mikami, T. Adachi, Y. Katayama, K. Tsuji, H. Kawamura, O. Shimomura, T. Nakajima, Phase transitions and superconductivity of black phosphorus and phosphorus-arsenic alloys at low temperatures and high pressures, Phys. Rev. B 50 (1994) 16274–16278.
[55]. W. Zhang, A.R. Oganov, A.F. Goncharov, Q. Zhu, S.E. Boulfelfel, A.O. Lyakhov, E. Stavrou, M. Somayazulu, V.B. Prakapenka, Z. Konôpková, Unexpected stable stoichiometries of sodium chlorides, Science 342 (2013) 1502–1505.
[56]. D.L.V.K. Prasad, N.W. Ashcroft, R. Hoffmann, Evolving structural diversity and metallicity in compressed lithium azide, J. Phys. Chem. C 117 (2013) 20838–20846.
[57]. J. Zhang, Z. Zeng, H.-Q. Lin, Y.-L. Li, Pressure-induced planar N_6 rings in potassium azide, Sci. Rep. 4 (2014) 4358.
[58]. S.B. Schneider, R. Frankovsky, W. Schnick, Synthesis of alkaline Earth diazenides M_{AEN2} (M_{AE} = Ca, Sr, Ba) by controlled thermal decomposition of azides under high pressure, Inorg. Chem. 51 (2012) 2366–2373.
[59]. S.B. Schneider, R. Frankovsky, W. Schnick, High-pressure synthesis and characterization of the alkali diazenide Li_2N_2, Angew. Chem. Int. Ed. 51 (2012) 1873–1875.
[60]. Y.-L. Li, W. Luo, Z. Zeng, H.-Q. Lin, H.K. Mao, R. Ahuja, Pressure-induced superconductivity in CaC_2, Proc. Natl. Acad. Sci. U.S.A. 110 (2013) 9289–9294.
[61]. Y.-L. Li, S.-N. Wang, A.R. Oganov, H. Gou, J.S. Smith, T.A. Strobel, Investigation of exotic stable calcium carbides using theory and experiment, Nat. Commun. 6 (2015) 6974.
[62]. O.O. Kurakevych, T.A. Strobel, D.Y. Kim, G.D. Cody, Synthesis of Mg_2C: a magnesium methanide, Angew. Chem. Int. Ed. 52 (2013) 8930–8933.
[63]. P. Srepusharawoot, A. Blomqvist, C.M. Araujo, R.H. Scheicher, R. Ahuja, One-dimensional polymeric carbon structure based on five-membered rings in alkaline Earth metal dicarbides BeC_2 and MgC_2, Phys. Rev. B 82 (2010) 125439.
[64]. I. Efthimiopoulos, K. Kunc, G.V. Vazhenin, E. Stavrou, K. Syassen, M. Hanfland, S. Liebig, U. Ruschewitz, Structural transformation and vibrational properties of BaC_2 at high pressure, Phys. Rev. B 85 (2012) 134125.
[65]. J. Nylen, S. Konar, P. Lazor, D. Benson, U. Haussermann, Structural behavior of the acetylide carbides Li_2C_2 and CaC_2 at high pressure, J. Chem. Phys. 137 (2012) 224507.
[66]. J. Catafesta, J. Haines, J.E. Zorzi, A.S. Pereira, C.A. Perottoni, Pressure-induced amorphization and decomposition of $Fe[Co(CN)_6]$, Phys. Rev. B 77 (2008) 064104.
[67]. Y. Moritomo, M. Hanawa, Y. Ohishi, K. Kato, M. Takata, A. Kuriki, E. Nishibori, M. Sakata, S. Ohkoshi, H. Tokoro, K. Hashimoto, Pressure- and photoinduced transformation into a metastable phase in $RbMn[Fe(CN)_6]$, Phys. Rev. B 68 (2003) 144106.
[68]. K. Li, H. Zheng, I.N. Ivanov, M. Guthrie, Y. Xiao, W. Yang, C.A. Tulk, Y. Zhao, H.K. Mao, $K_3Fe(CN)_6$: pressure-induced polymerization and enhanced conductivity, J. Phys. Chem. C 117 (2013) 24174–24180.
[69]. L.F. Lundegaard, G. Weck, M.I. McMahon, S. Desgreniers, P. Loubeyre, Observation of an O_8 molecular lattice in the ε phase of solid oxygen, Nature 443 (2006) 201–204.
[70]. Y. Meng, P.J. Eng, J.S. Tse, D.M. Shaw, M.Y. Hu, J. Shu, S.A. Gramsch, C. Kao, R.J. Hemley, H.K. Mao, Inelastic X-ray scattering of dense solid oxygen: evidence for intermolecular bonding, Proc. Nat. Acad. Sci. USA 105 (2008) 11640–11644.
[71]. M.I. Eremets, A.G. Gavriliuk, I.A. Trojan, D.A. Dzivenko, R. Boehler, Single-bonded cubic form of nitrogen, Nat. Mater. 3 (2004) 558–563.
[72]. W.J. Evans, M.J. Lipp, C.-S. Yoo, H. Cynn, J.L. Herberg, R.S. Maxwell, M.F. Nicol, Pressure-induced polymerization of carbon monoxide: disproportionation and synthesis of an energetic lactonic polymer, Chem. Mater. 18 (2006) 2520–2531.
[73]. A.L. Katz, D. Schiferl, R.L. Mills, New phases and chemical reactions in solid CO under pressure, J. Phys. Chem. 88 (1984) 3176–3179.
[74]. F. Datchi, B. Mallick, A. Salamat, S. Ninet, Structure of polymeric carbon dioxide CO_2-V, Phys. Rev. Lett. 108 (2012) 125701.
[75]. M. Santoro, F.A. Gorelli, R. Bini, J. Haines, O. Cambon, C. Levelut, J.A. Montoya, S. Scandolo, Partially collapsed cristobalite structure in the non molecular phase V in CO_2, Proc. Natl. Acad. Sci. U.S.A. 109 (2012) 5176–5179.
[76]. V. Iota, C.-s. Yoo, J.-H. Klepeis, Z. Jenei, W. Evans, H. Cynn, Six-fold coordinated carbon dioxide VI, Nat. Mater. 6 (2007) 34–38.
[77]. P. Pruzan, J.C. Chervin, M.M. Thiery, J.P. Itie, J.M. Besson, J.P. Forgerit, M. Revault, Transformation of benzene to a polymer after static pressurization to 30 GPa, J. Chem. Phys. 92 (1990) 6910–6915.
[78]. B.R. Jackson, C.C. Trout, J.V. Badding, UV Raman analysis of the C:H network formed by compression of benzene, Chem. Mater. 15 (2003) 1820–1824.
[79]. T.C. Fitzgibbons, M. Guthrie, E.-s. Xu, V.H. Crespi, S.K. Davidowski, G.D. Cody, N. Alem, J.V. Badding, Benzene-derived carbon nanothreads, Nat. Mater. 14 (2015) 43–47.

[80]. M. Citroni, R. Bini, P. Foggi, V. Schettino, Role of excited electronic states in the high-pressure amorphization of benzene, Proc. Natl. Acad. Sci. USA 105 (2008).
[81]. L. Ciabini, M. Santoro, F.A. Gorelli, R. Bini, V. Schettino, S. Raugei, Triggering dynamics of the high-pressure benzene amorphization, Nat. Mater. 6 (2007) 39−43.
[82]. K. Aoki, S. Usuba, M. Yoshida, Y. Kakudate, K. Tanaka, S. Fujiwara, Raman-study of the solid-state polymerization of acetylene at high-pressure, J. Chem. Phys. 89 (1988) 529−534.
[83]. C.C. Trout, J.V. Badding, Solid state polymerization of acetylene at high pressure and low temperature, J. Phys. Chem. A 104 (2000) 8142−8145.
[84]. M. Ceppatelli, M. Santoro, R. Bini, V. Schettino, Fourier transform infrared study of the pressure and laser induced polymerization of solid acetylene, J. Chem. Phys. 113 (2000) 5991−6000.
[85]. M. Sakashita, H. Yamawaki, K. Aoki, FT-IR study of the solid state polymerization of acetylene under pressure, J. Phys. Chem. 100 (1996) 9943−9947.
[86]. K. Aoki, Y. Kakudate, M. Yoshida, S. Usuba, S. Fujiwara, Solid-state polymerization of cyanoacetylene into conjugated linear-chains under pressure, J. Chem. Phys. 91 (1989) 778−782.
[87]. M. Santoro, L. Ciabini, R. Bini, V. Schettino, High-pressure polymerization of phenylacetylene and of the benzene and acetylene moieties, J. Raman Spectrosc. 34 (2003) 557−566.
[88]. K. Aoki, B.J. Baer, H.C. Cynn, M. Nicol, High-pressure Raman-study of one-dimensional crystals of the very polar molecule hydrogen-cyanide, Phys. Rev. B 42 (1990) 4298−4303.
[89]. V. Schettino, R. Bini, Molecules under extreme conditions: chemical reactions at high pressure, Phys. Chem. Chem. Phys. 5 (2003) 1951−1965.
[90]. M. Citroni, M. Ceppatelli, R. Bini, V. Schettino, Laser-induced selectivity for dimerization versus polymerization of butadiene under pressure, Science 295 (2002) 2058−2060.
[91]. M.S. Paterson, Rock deformation experimentation. The Brittle-Ductile Transition in Rocks, American Geophysical Union, 1990, pp. 187−194.
[92]. T.N. Tingle, H.W. Green II, T.E. Young, T.A. Koczynski, Improvements to Griggs-type apparatus for mechanical testing at high pressures and temperatures, Pure Appl. Geophys. 141 (1993) 523−543.
[93]. J.H. Chen, L. Li, D. Weidner, M. Vaughan, Deformation experiments using synchrotron X-rays: in situ stress and strain measurements at high pressure and temperature, Phys. Earth Planet. Inter. 143−44 (2004) 347−356.
[94]. Y.B. Wang, W.B. Durham, I.C. Getting, D.J. Weidner, The deformation-DIA: a new apparatus for high temperature triaxial deformation to pressures up to 15 GPa, Rev. Sci. Instrum. 74 (2003) 3002−3011.
[95]. S.A. Hunt, D.J. Weidner, R.J. McCormack, M.L. Whitaker, E. Bailey, L. Li, M.T. Vaughan, D.P. Dobson, Deformation T-Cup: a new multi-anvil apparatus for controlled strain-rate deformation experiments at pressures above 18 GPa, Rev. Sci. Instrum. 85 (2014) 085103.
[96]. T. Kawazoe, T. Ohuchi, N. Nishiyama, Y. Nishihara, T. Irifune, Preliminary deformation experiment of ringwoodite at 20 GPa and 1 700 K using a D-DIA apparatus, J. Earth Sci. 21 (2010) 517−522.
[97]. Y. Nishihara, D. Tinker, T. Kawazoe, Y. Xu, Z. Jing, K.N. Matsukage, S.-i. Karato, Plastic deformation of wadsleyite and olivine at high-pressure and high-temperature using a rotational Drickamer apparatus (RDA), Phys. Earth Planet. Inter. 170 (2008) 156−169.
[98]. J.-P. Poirier, Creep of Crystals: High-temperature Deformation Processes in Metals, Ceramics and Minerals, Cambridge University Press, Cambridge, 1985, p. 276.
[99]. P.N. Chopra, M.S. Paterson, The experimental deformation of dunite, Tectonophys 78 (1981) 453−473.
[100]. S. Mei, D.L. Kohlstedt, Influence of water on plastic deformation of olivine aggregates 2. Dislocation creep regime, J. Geophys. Res. 105 (2000) 21471−21481.
[101]. G. Hirth, D. Kohlstedt, Rheology of the upper mantle and the mantle wedge: a view from the experimentalists, in: J. Eiler (Ed.), Inside the Subduction Factory, American Geophysical Union, 2003, pp. 83−105.
[102]. S.-I. Karato, H. Jung, Effects of pressure on high-temperature dislocation creep in olivine, Philos. Mag. 83 (2003) 401−414.
[103]. T. Kawazoe, S.-i. Karato, K. Otsuka, Z. Jing, M. Mookherjee, Shear deformation of dry polycrystalline olivine under deep upper mantle conditions using a rotational Drickamer apparatus (RDA), Phys. Earth Planet. Inter. 174 (2009) 128−137.
[104]. W.B. Durham, S. Mei, D.L. Kohlstedt, L. Wang, N.A. Dixon, New measurements of activation volume in olivine under anhydrous conditions, Phys. Earth Planet. Inter. 172 (2009) 67−73.
[105]. L. Li, D. Weidner, P. Raterron, J. Chen, M. Vaughan, S. Mei, B. Durham, Deformation of olivine at mantle pressure using the D-DIA, Eur. J. Mineral. 18 (2006) 7−19.
[106]. P. Raterron, J. Chen, L. Li, D. Weidner, P. Cordier, Pressure-induced slip-system transition in forsterite: single-crystal rheological properties at mantle pressure and temperature, Am. Mineral. 92 (2007) 1436−1445.
[107]. N. Hilairet, Y. Wang, T. Sanehira, S. Merkel, S. Mei, Deformation of olivine under mantle conditions: an in situ high-pressure, high-temperature study using monochromatic synchrotron radiation, J. Geophys. Res. 117 (2012) B01203.
[108]. S.-i. Karato, Rheology of the deep upper mantle and its implications for the preservation of the continental roots: a review, Tectonophys 481 (2010) 82−98.
[109]. J.V. Ross, G.A.L. Hans, N.L. Carter, Activation volume for creep in the upper mantle, Science 203 (1979) 261−263.
[110]. H.W. Green II, R.S. Borch, The pressure dependence of creep, Acta Metall. 35 (1987) 1301−1305.
[111]. F. Béjina, P. Raterron, J. Zhang, O. Jaoul, R.C. Liebermann, Activation volume of silicon diffusion in San Carlos olivine, Geophys. Res. Lett. 24 (1997) 2597−2600.
[112]. P. Raterron, E. Amiguet, J. Chen, L. Li, P. Cordier, Experimental deformation of olivine single crystals at mantle pressures and temperatures, Phys. Earth Planet. Inter. 172 (2009) 74−83.
[113]. S.-I. Karato, D.C. Rubie, H. Yan, Dislocation recovery in olivine under deep upper mantle conditions: Implications for creep and diffusion, J. Geophys. Res. 98 (1993) 9761−9768.
[114]. D.L. Kohlstedt, H.P.K. Nichols, P. Hornack, The effect of pressure on the rate of dislocation recovery in olivine, J. Geophys. Res. 85 (1980) 3122−3130.
[115]. S.-I. Karato, Comment on 'The effect of pressure on the rate of dislocation recovery in olivine' by D. L. Kohlstedt, H. P. K. Nichols, and Paul Hornack, J. Geophys. Res. 86 (1981) 9319.
[116]. S. Karato, M. Ogawa, High-pressure recovery of olivine: implications for creep mechanisms and creep activation volume, Phys. Earth Planet. Inter. 28 (1982) 102−117.
[117]. S.-i. Karato, D.C. Rubie, Toward an experimental study of deep mantle rheology: a new multianvil sample assembly for deformation studies under high pressures and temperatures, J. Geophys. Res. 102 (1997) 20111−20122.
[118]. K.S. Kumar, S. Suresh, M.F. Chisholm, J.A. Horton, P. Wang, Deformation of electrodeposited nanocrystalline nickel, Acta Mater. 51 (2003) 387−405.
[119]. Z.W. Shan, J.M.K. Wiezorek, E.A. Stach, D.M. Follstaedt, J.A. Knapp, S.X. Mao, Dislocation dynamics in nanocrystalline nickel, Phys. Rev. Lett. 98 (2007) 095502.
[120]. M. Chen, E. Ma, K.J. Hemker, H. Sheng, Y. Wang, X. Cheng, Deformation twinning in nanocrystalline aluminum, Science 300 (2003) 1275−1277.
[121]. X. Li, Y. Wei, L. Lu, K. Lu, H. Gao, Dislocation nucleation governed softening and maximum strength in nano-twinned metals, Nature 464 (2010) 877−880.
[122]. L. Lu, X. Chen, X. Huang, K. Lu, Revealing the maximum strength in nanotwinned copper, Science 323 (2009) 607−610.
[123]. V. Yamakov, D. Wolf, S.R. Phillpot, A.K. Mukherjee, H. Gleiter, Dislocation processes in the deformation of nanocrystalline aluminium by molecular-dynamics simulation, Nat. Mater. 1 (2002) 45−48.
[124]. R.L. Penn, J.F. Banfield, Imperfect oriented attachment: dislocation generation in defect-free nanocrystals, Science 281 (1998) 969−971.

[125]. J. Schiøtz, K.W. Jacobsen, A maximum in the strength of nanocrystalline copper, Science 301 (2003) 1357–1359.
[126]. J. Schiøtz, F.D.D. Tolla, K.W. Jacobsen, Softening of nanocrystalline metals at very small grain sizes, Nature 391 (1998) 561–563.
[127]. B. Chen, K. Lutker, S.V. Raju, J. Yan, W. Kanitpanyacharoen, J. Lei, S. Yang, H.-R. Wenk, H.K. Mao, Q. Williams, Texture of nanocrystalline nickel: probing the lower size limit of dislocation activity, Science 338 (2012) 1448–1451.
[128]. Z. Shan, E.A. Stach, J.M.K. Wiezorek, J.A. Knapp, D.M. Follstaedt, S.X. Mao, Grain boundary–mediated plasticity in nanocrystalline nickel, Science 305 (2004) 654–657.
[129]. W.J. Clegg, Controlling cracks in ceramics, Science 286 (1999) 1097–1099.
[130]. J. Karch, R. Birringer, H. Gleiter, Ceramics ductile at low temperature, Nature 330 (1987) 556–558.
[131]. S-i Karato, Deformation of Earth Materials: an Introduction to the Rheology of Solid Earth, Cambridge University Press, Cambridge, 2008.
[132]. S. Tateno, K. Hirose, Y. Ohishi, Y. Tatsumi, The structure of iron in Earth's inner core, Science 330 (2010) 359–361.
[133]. J. Bhattacharyya, P. Shearer, G. Masters, Inner core attenuation from short-period PKP(BC) versus PKP(DF) waveforms, Geophys. J. Intl. 114 (1993) 1–11.
[134]. X. Song, Anisotropy of the Earth's inner core, Rev. Geophys. 35 (1997) 297–313.
[135]. J. Tromp, Inner-core anisoropy and rotation, Annu. Rev. Earth Planet. Sci. 29 (2001) 47–69.
[136]. L. Wen, F. Niu, Seismic velocity and attenuation structures in the top of the Earth's inner-core, J. Geophys. Res. 107 (2002), http://dx.doi.org/10.1029/2001JB000170.
[137]. S. Merkel, H.-R. Wenk, P. Gillet, H.K. Mao, R.J. Hemley, Deformation of polycrystalline iron up to 30 GPa and 1000 K, Phys. Earth Planet. Inter. 145 (2004) 239–251.
[138]. L. Miyagi, M. Kunz, J. Knight, J. Nasiatka, M. Voltolini, H.-R. Wenk, In situ phase transformation and deformation of iron at high pressure and temperature, J. Appl. Phys. 104 (2008) 103510.
[139]. L. Miyagi, W. Kanitpanyacharoen, P. Kaercher, K.K.M. Lee, H.-R. Wenk, Slip systems in $MgSiO_3$ post-perovskite: implications for D″ anisotropy, Science 329 (2010) 1639–1641.
[140]. S. Merkel, A. Kubo, L. Miyagi, S. Speziale, T.S. Duffy, H.K. Mao, H.-R. Wenk, Plastic deformation of $MgGeO_3$ post-perovskite at lower mantle pressures, Science 311 (2006) 644–646.
[141]. J. Trampert, HJv Heijst, Global azimuthal anisotropy in the transition zone, Science 296 (2002) 1297–1299.
[142]. S.-i. Karato, A dislocation model of seismic wave attenuation and micro-creep in the Earth: Harold Jeffreys and the rheology of the solid Earth, Pure Appl. Geophys. 153 (1998) 239–256.
[143]. J. Chen, T. Inoue, D.J. Weidner, Y. Wu, M.T. Vaughan, Strength and water weakening of mantle minerals, olivine, wadsleyite and ringwoodite, Geophys. Res. Lett. 25 (1998) 575–578.
[144]. T. Kubo, E. Ohtani, T. Kato, T. Shinmei, K. Fujino, Effects of water on the α-β transformation kinetics in San Carlos olivine, Science 281 (1998) 85–87.
[145]. R. Jeanloz, P.M. Celliers, G.W. Collins, J.H. Eggert, K.K.M. Lee, R.S. McWilliams, S. Brygoo, P. Loubeyre, Achieving high-density states through shock-wave loading of precompressed samples, Proc. Natl. Acad. Sci. USA 104 (2007) 9172–9177.
[146]. M. Millot, N. Dubrovinskaia, A. Černok, S. Blaha, L. Dubrovinsky, D.G. Braun, P.M. Celliers, G.W. Collins, J.H. Eggert, R. Jeanloz, Shock compression of stishovite and melting of silica at planetary interior conditions, Science 347 (2015) 418–420.
[147]. R.F. Smith, J.H. Eggert, R. Jeanloz, T.S. Duffy, D.G. Braun, J.R. Patterson, R.E. Rudd, J. Biener, A.E. Lazicki, A.V. Hamza, J. Wang, T. Braun, L.X. Benedict, P.M. Celliers, G.W. Collins, Ramp compression of diamond to five terapascals, Nature 511 (2014) 330–333.
[148]. K.K.M. Lee, L.R. Benedetti, R. Jeanloz, P.M. Celliers, J.H. Eggert, D.G. Hicks, S.J. Moon, A. Mackinnon, G.W. Collins, E. Henry, M. Koenig, A. Benuzzi-Mounaix, Laser-driven shock experiments on precompressed water: implications for "icy" giant planets, J. Chem. Phys. 125 (2006) 14701.
[149]. J.H. Eggert, S. Brygoo, P. Loubeyre, R.S. McWilliams, P.M. Celliers, D.G. Hicks, T.R. Boehly, R. Jeanloz, G.W. Collins, Hugoniot data for helium in the ionization regime, Phys. Rev. Lett. 100 (2008) 124503.
[150]. P.M. Celliers, P. Loubeyre, J.H. Eggert, S. Brygoo, R.S. McWilliams, D.G. Hicks, T.R. Boehly, R. Jeanloz, G.W. Collins, Insulator-to-conducting transition in dense fluid helium, Phys. Rev. Lett. 104 (2010) 184503.
[151]. P. Loubeyre, S. Brygoo, J. Eggert, P.M. Celliers, D.K. Spaulding, J.R. Rygg, T.R. Boehly, G.W. Collins, R. Jeanloz, Extended data set for the equation of state of warm dense hydrogen isotopes, Phys. Rev. B 86 (2012) 144115.
[152]. M.D. Knudson, M.P. Desjarlais, A. Becker, R.W. Lemke, K.R. Cochrane, M.E. Savage, D.E. Bliss, T.R. Mattsson, R. Redmer, Direct observation of an abrupt insulator-to-metal transition in dense liquid deuterium, Science 348 (2015) 1455–1460.
[153]. A.P. Drozdov, M.I. Eremets, I.A. Troyan, V. Ksenofontov, S.I. Shylin, Conventional superconductivity at 203 kelvin at high pressures in the sulfur hydride system, Nature 525 (2015) 73–76.
[154]. Q. Huang, D. Yu, B. Xu, W. Hu, Y. Ma, Y. Wang, Z. Zhao, B. Wen, J. He, Z. Liu, Y. Tian, Nanotwinned diamond with unprecedented hardness and stability, Nature 510 (2014) 250–253.
[155]. T. Irifune, A. Kurio, S. Sakamoto, T. Inoue, H. Sumiya, Ultrahard polycrystalline diamond from graphite, Nature 421 (2003) 599–600.